Compressive Sensing with Low Precision Data Representation: Radio Astronomy and Beyond

Nezihe Merve Gürel*, Kaan Kara*, Dan Alistarh† and Ce Zhang*

Department of Computer Science ETH Zurich

e-mail: nezihe.guerel@inf.ethz.ch, kaan.kara@inf.ethz.ch, ce.zhang@inf.ethz.ch

Institute of Science and Technology IST Austria e-mail: dan.alistarh@ist.ac.at

Abstract: Modern scientific instruments produce vast amounts of data, which can overwhelm the processing ability of computer systems. Lossy compression of data is an intriguing solution, but comes with its own dangers, such as potential signal loss, and the need for careful parameter optimization. In this work, we focus on a setting where this problem is especially acute—compressive sensing frameworks for radio astronomy—and ask: Can the precision of the data representation be lowered for <u>all</u> input data, with recovery guarantees and good practical performance?

Our first contribution is a theoretical analysis of the Iterative Hard Thresholding (IHT) algorithm when all input data, that is, the measurement matrix and the observation, are quantized aggressively, to as little as 2 bits per value. Under reasonable constraints, we show that there exists a variant of low precision IHT which can still provide recovery guarantees. The second contribution is a tailored analysis of our general quantized framework to radio astronomy, showing that its conditions are satisfied in this case. We evaluate our approach using an FPGA implementation, and show that it can achieve up to $9.19\times$ speed up with negligible loss of recovery quality, on real telescope data.

1. Introduction

The ability to collect, store, and process large amount of data is enabling a next generation of *data intensive* scientific instruments. For example, the Square Kilometre Array (SKA), the largest radio telescope ever built, has thousands of dishes, and is expected to achieve raw data throughput of 62 Exabytes by mid-2020. Such instruments require extremely advanced capabilities in terms of engineering, algorithms, calibration, and storage (Hu & Kaabouch, 2014).

In this paper, we focus on compressive sensing (Donoho, 2006; Candes et al., 2006a,b), a popular mathematical framework behind many of these instruments. Particularly, we want to understand the impact of representing all input data in lower precision, instead of 32-bit floating-point values. We make the following contributions:

^{*}ETH Zurich

 $^{^\}dagger \mathrm{IST}$ Austria

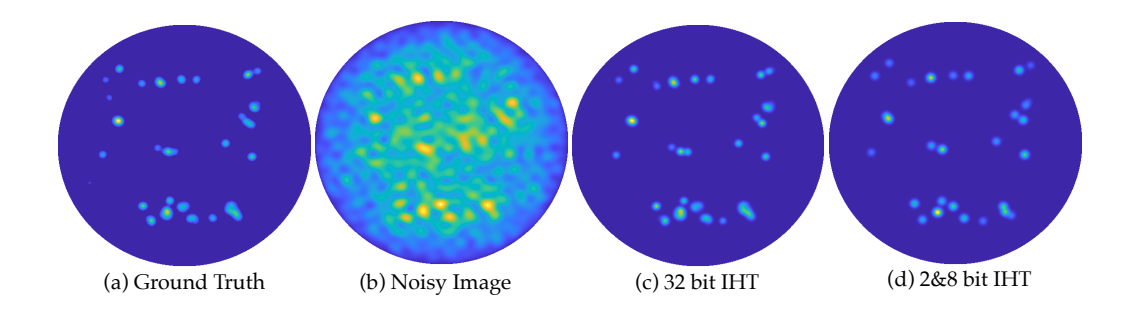


Fig 1. Illustration of the main results of this paper. Representing all input data at low precision, Iterative Hard Thresholding gets negligible loss of recovery quality (data from LOFAR station CS302, 2 bit measurement matrix and 8 bit observation). This paper provides both the analysis, and the system implementation.

- 1. We develop a theoretical framework, which shows for the first time that, under certain technical conditions, Iterative Hard Thresholding (IHT), a popular algorithm for compressive sensing, converges with guarantees on the recovery quality when all input data is in lower precision.
- 2. We refine our results in the context of a radio astronomy application formulated in the context of compressive sensing, and develop *stronger* application-specific guarantees for sky recovery by leveraging the properties of the measurement matrix in this scenario.
- 3. We evaluate our approach on an FPGA-based implementation that achieves up to 9.19× speed-up to recovery, on problems with a dense measurement matrix quantized to 2-bit precision, and with 8-bit observations. We believe this approach can further generalize to other sparse reconstruction problems demanding high processing capability, with similar speedups.

1.1. Problem Formulation

Compressive sensing (CS) (Donoho, 2006; Candes et al., 2006a,b) is a foundational technique in sparse signal reconstruction. CS offers a range of efficient algorithms acquiring high dimensional signals from inaccurate and incomplete samples with an underlying sparse structure. Many real-life problems, e.g, medical imaging, interferometry, video, spectroscopy and genomic data analysis, can benefit from these techniques.

In mathematical terms, CS is formulated as follows. Let a sparse or approximately sparse signal $\mathbf{x} \in \mathbb{R}^N$ be sampled via a linear sampling operator $\mathbf{\Phi}^{M \times N}$. In matrix notation, the vector of measurements $\mathbf{y} \in \mathbb{C}^M$ is

$$\mathbf{y} = \mathbf{\Phi}\mathbf{x} + \mathbf{e} \tag{1}$$

where **e** is the observation noise and M < N.

CS recovery algorithms iteratively build up a sparse estimate \mathbf{x} such that $\mathbf{\Phi}\mathbf{x}$ approximates \mathbf{y} well, that is, $\|\mathbf{y} - \mathbf{\Phi}\mathbf{x}\|_2$ is small. The sparsity constraint imposed on \mathbf{x} overcomes this

ill-posed problem, yet is computationally NP-hard due to its combinatorial nature. Therefore, most CS algorithms resort to convex relaxation of ℓ_0 -based optimization, or a collection of thresholding and greedy methods such as Iterative Hard Thresholding (IHT) (Blumensath & Davies, 2008, 2009) and Compressive Sampling Matching Pursuit (CoSaMP) (Neededl & Tropp, 2008). The past decade has seen significant work on such methods, see (Liu et al., 2017; Yuan et al., 2014, 2016; Blumensath, 2013; Neededl & Tropp, 2008) and references therein. These references present an comprehensive analysis of the provable performance guarantees for such sparsity-constrained minimization methods, in terms of convergence to fixed points of ℓ_0 -regularized cost functions and the optimality of such approximations. However, these frameworks face several challenges when applied to real-life problems: for provable guarantees, it is often required that (1) the measurement matrix Φ satisfies the Restricted Isometry Property (RIP) (Candes, 2008; Chartrand & Staneva, 2008), and that (2) the sparsity level is chosen appropriately. Normalized IHT (NIHT) (Blumensath & Davies, 2010), is a simple yet very effective strategy which relieves some of the limitations listed above: a step size parameter is introduced to the traditional IHT (Blumensath & Davies, 2008). This simple refinement alleviates the RIP condition imposed on Φ , enabling rigorous guarantees for a broader class of practical problems. This paper builds upon this line of work.

Problem Formulation We consider the sparse signal recovery problem in Eqn. (1) described as: given \mathbf{y} and $\mathbf{\Phi}$, find coefficients \mathbf{x} minimizing the cost function

$$\|\mathbf{y} - \mathbf{\Phi}\mathbf{x}\|_2^2 \text{ subject to } \|\mathbf{x}\|_0 \le s,$$
 (2)

where $\|\mathbf{x}\|_0 = |\text{supp}(\mathbf{x})| = |\{i : x_i \neq 0\}|.$

Under certain constraints, normalized IHT is guaranteed to approximate \mathbf{x} with high accuracy. Here, we consider the properties of this algorithm in a lossy compression setting, where the data \mathbf{y} and $\mathbf{\Phi}$ consisting of floating-point values undergo a stochastic quantization process to a small set of integer levels denoted by Q. The goal of Q is to reduce the extremely high cost of data transmission. That is, we wish to recover \mathbf{x} using the modified NIHT update rule:

$$\mathbf{x}^{[n+1]} = H_s(\mathbf{x}^{[n]} + \mu^{[n]}Q(\mathbf{\Phi})(Q(\mathbf{y}) - Q(\mathbf{\Phi})\mathbf{x}^{[n]}))$$
(3)

where $H_s(\mathbf{x}): \mathbb{C}^n \to \mathbb{C}^n$ the nonlinear operator that preserves the largest s (in magnitude) entries of \mathbf{x} and sets the rest to zero.

2. Related work

Using a low precision data representation in the context of compressive sensing is not new. In fact, a series of studies made successive attempts to apply low precision to compressive sensing problems, summarized in Fig. 2. (Boufounos & Baraniuk, 2009) demonstrate that sparse signals can be recovered with a scale factor when measurements preserve only sign information. (Ai et al., 2012; Davenport et al., 2012) show that approximately sparse signals can be robustly recovered from single-bit measurements sampled with a sub-Gaussian distribution. (Jacques et al., 2012; Laska et al., 2011) study the similar setting with a Gaussian measurement matrix, the so called Binary IHT. (Plan & Vershynin, 2011, 2012) propose

	Assumption on Φ	$Q(\Phi)$	Q(y)
Boufounos et al.	Gaussian	×	√
Ai et al.	unit variance	×	\checkmark
Jacques et al.	RIP	×	\checkmark
Laska et al.	Gaussian & RIP	×	\checkmark
Plan et al. (2011)	Gaussian & RIP	×	\checkmark
Plan et al. (2012)	Gaussian	×	\checkmark
Gupta et al.	Gaussian	×	\checkmark
Gopi et al.	sub-Gaussian/binary & RIP	✓	\checkmark
This Paper	non-symmetric RIP	√	√

Fig 2. Comparison of This Paper with Previous Work. $Q(\Phi)$ and Q(y) means whether the paper considers quantizing Φ and y, respectively (\checkmark means yes).

a computationally tractable and optimal recovery of 1-bit compressive sensing problem. (Gupta et al., 2010; Gopi et al., 2013) present provable theoretical guarantees to identify support recovery of high dimensional sparse signals for 1-bit measurements.

This paper differs from these references in two ways: First, as we discuss in Section 4, our assumption that the measurement matrix being non-symmetric RIP is critical in radio astronomy applications, and none of these assumptions made by previous work would fit this use case. Second, we are the only work, with the exception of (Gopi et al., 2013), that quantizes both the measurement matrix Φ and the observations. (Gopi et al., 2013) considers the problem of building a binary measurement matrix which can provide good support recovery guarantees given only one-bit measurements; by contrast, we consider a practical setting where we must quantize a given full-precision measurement matrix as well as possible, and can trade off higher precision for better recovery guarantees. We discuss the system-side benefits of quantizing the matrix Φ in Section 4.4.

Another emerging line of work has been on low precision training for machine learning applications beyond compressive sensing. Examples include Buckwild! (Sa et al., 2015), QSGD (Alistarh et al., 2016), ZipML (Zhang et al., 2017), and a series of works about partial or end-to-end low-precision training of deep learning models (Seide et al., 2014; Hubara et al., 2016; Rastegari et al., 2016; Zhou et al., 2016b,a; Li et al., 2016; Gupta et al., 2013). Most of these works are designed for stochastic gradient descent (SGD). In this paper, we go beyond SGD, and focus on compressive sensing.

Another rich line of research is on designing efficient algorithms for sparse recovery problems (Blumensath, 2012; Wei, 2015; Blanchard et al., 2013; Cevher, 2011; Liu et al., 2017). We focus here on normalized IHT, and leave extensions to other recovery methods as future work.

3. Preliminaries

In this section, we review the preliminary results on the normalized IHT (NIHT) algorithm introduced by (Blumensath & Davies, 2010; Blumensath et al., 2012).

Notation: Scalars are denoted by italics, vectors by bold lower-case and matrices by bold upper-case. For all $\mathbf{x} = (x_1, ..., x_N) \in \mathbb{R}^N$, we denote by $\|\mathbf{x}\|_p$ the standard operator norm. Let $\Phi_{m,n} \in \mathbb{C}^{M \times N}$ denote the matrix element in the m'th row and n'th column. Finally 32 bit denotes the full precision scheme and $b_{\Phi} \& b_{\mathbf{y}}$ bit precision denote the number of bits used to represent the measurement matrix Φ and vector of observations \mathbf{y} , respectively.

3.1. Iterative Hard Thresholding

Let $\mathbf{x}^{[0]} = 0$. Normalized IHT has the following update rule per iteration:

$$\mathbf{x}^{[n+1]} = H_s(\mathbf{x}^{[n]} + \mu^{[n]}\mathbf{\Phi}(\mathbf{y} - \mathbf{\Phi}\mathbf{x}^{[n]})),\tag{4}$$

where $\mu^{[n]} > 0$ is the adaptive step size parameter, and $H_s(\mathbf{x})$ is the thresholding operator that preserves the largest s (in magnitude) entries.

3.2. Convergence

The analysis of hard thresholding algorithms heavily relies on the scaling properties of Φ . More precisely, the convergence to a local minimum of the cost function Eqn. 2 as well as the quality of such approximation are proven under certain conditions on Φ . More concretely, one must often deal with non-symmetric Restricted Isometry Property (RIP) condition: a matrix Φ satisfies non-symmetric RIP if

$$\alpha_s \le \frac{\|\mathbf{\Phi}\mathbf{x}\|_2}{\|\mathbf{x}\|_2} \le \beta_s \tag{5}$$

for all $\mathbf{x} : \|\mathbf{x}\|_0 \le s$, and where $0 < \alpha_s, \beta_s \in \mathbb{R}$, $\alpha_s \le \beta_s$, the so-called Restricted Isometric Constants (RICs), are lower and upper singular values of $\mathbf{\Phi}$, respectively.

Remark 1. The convergence of normalized IHT depends conditionally on the step size parameter $\mu^{[n]}$, unlike the traditional IHT approach where $\mu^{[n]} = 1$. While the traditional approach requires a re-scaling of the measurement matrix such that $\|\mathbf{\Phi}\|_2 < 1$ to ensure convergence, introducing a step size parameter enables the arbitrary scaling of $\mathbf{\Phi}$ hence relaxing the bounds on its norm. The role of $\mu^{[n]}$ here is to compensate for this re-scaling by accordingly avoiding the undesirable amplification of noise, i.e., the ratio $\|\mathbf{\Phi}\mathbf{x}\|_2/\|\mathbf{e}\|_2$ remains unchanged.

The main convergence result can be stated as follows.

Theorem 1. (Blumensath et al., 2012)

Let Φ be full rank, and $s \leq m$. If $\beta_{2s} \leq \mu^{-1}$, then NIHT converges to a local minimum of Eqn. 2.

3.3. Step Size Determination

When setting the step size parameter, the condition that $\beta_{2s} \leq \mu^{-1}$, which ensures convergence, poses the following challenge. To date, there is no universal strategy to check if

the RIP holds for an arbitrary measurement matrix in a computationally efficient manner. A similar discussion holds for attaining the RICs, i.e., β_s and α_s , associated with the measurement matrix Φ . It can however be shown that, under certain conditions, randomly constructed measurement matrices can satisfy the RIP with high probability (Candes, 2008; Chartrand & Staneva, 2008). Still, this remains a bottleneck for a more general class of measurement matrices. Without losing the main track, we briefly review generic strategies for step size determination.

If the support is fixed, a natural strategy to set the step size adaptively is (Blumensath & Davies, 2010)

$$\mu^{[n]} = \frac{\mathbf{g}_{\Gamma^{[n]}}^T \mathbf{g}_{\Gamma^{[n]}}}{\mathbf{g}_{\Gamma^{[n]}}^T \mathbf{\Phi}_{\Gamma^{[n]}}^T \mathbf{g}_{\Gamma^{[n]}}}$$
(6)

where $\mathbf{g}^{[n]} = \mathbf{\Phi}^T(\mathbf{y} - \mathbf{\Phi}\mathbf{x}^{[n]})$. Clearly, the maximal reduction in cost function can then be attained. However, if the support of $\mathbf{x}^{[n+1]}$ differs from that of $\mathbf{x}^{[n]}$, the sufficient convergence condition becomes

$$\mu^{[n]} \le (1 - c) \frac{\|\mathbf{x}^{[n+1]} - \mathbf{x}^{[n]}\|_2^2}{\|\mathbf{\Phi}(\mathbf{x}^{[n+1]} - \mathbf{x}^{[n]})\|_2^2},\tag{7}$$

for any small constant c.

If the above condition is not met, a new proposal for $\mathbf{x}^{[n+1]}$ can be calculated by using $\mu^{[n]} \leftarrow \mu^{[n]}/(k(1-c))$, where k is a shrinkage parameter such that k > 1/(1-c). This adaptive setting of step size parameter is shown to provide RIP-invariant convergence as follows.

Theorem 2. (Blumensath & Davies, 2010)

Consider a noisy observation $\mathbf{y} = \mathbf{\Phi}\mathbf{x} + \mathbf{e}$ with an arbitrary vector \mathbf{x} . If $rank(\mathbf{\Phi}) = m$ and $rank(\mathbf{\Phi}_{\Gamma}) = s$ $\forall \Gamma : |\Gamma| = s$, then the normalized IHT algorithm converges to a local minimum of the cost function Eqn. 2. Also, assume $\mathbf{\Phi}$ is non-symmetric RIP_{2s} and let $\gamma_{2s} = \beta_{2s}/\alpha_{2s} - 1$. If $\gamma_{2s} \leq 1/8$, then

$$\|\mathbf{x} - \mathbf{x}^n\|_2 \le 2^{-n} \|\mathbf{x}^s\|_2 + 8\epsilon_s \tag{8}$$

where

$$\epsilon_s = \|\mathbf{x} - \mathbf{x}^s\|_2 + \frac{\|\mathbf{x} - \mathbf{x}^s\|_1}{\sqrt{s}} + \frac{1}{\beta_{2s}} \|\mathbf{e}\|_2.$$
 (9)

After at most $n^* = \log_2(\|\mathbf{x}^s\|_2/\epsilon_s)$ iterations, the recovery error bound in Eqn. 8 can be further simplified to

$$\|\mathbf{x} - \mathbf{x}^n\|_2 < 9\epsilon_s. \tag{10}$$

The above result suggests that, after a sufficiently large number of iterations, the reconstruction error is induced only by the noise e and that x is not exactly s-sparse.

4. Low Precision Iterative Thresholding

In this section, we analyze the quantized version of IHT for its guarantee for signal recovery performance. The key development here is that, by reducing the bit widths of the data

Algorithm 1 Low Precision Iterative Thresholding

Input: The set of low precision measurement matrices $\{\hat{\Phi}_1, \hat{\Phi}_2, ... \hat{\Phi}_{2n^*}\}$, measurements $\hat{\mathbf{y}}$, sparsity parameter s, number of iterations n^* , step size tuning parameters k, c Initialize $\mathbf{x}^{[0]} = 0$, $\Gamma^{[1]} = \operatorname{supp}(\mathbf{H}_{\mathbf{s}}(\hat{\Phi}_1^{\dagger}\hat{\mathbf{y}}))$. for n=1 to n^* do $\mathbf{g}^{[n]} = \hat{\Phi}_{2n-1}(\hat{\mathbf{y}} - \hat{\Phi}_{2n}\mathbf{x}^{[n]})$ $\hat{\mu}^{[n]} = (\mathbf{g}_{\Gamma^{[n]}}^{\dagger} \mathbf{g}_{\Gamma^{[n]}})/(\mathbf{g}_{\Gamma^{[n]}}^{\dagger} \mathbf{\Phi}_{\Gamma^{[n]}}^{\dagger} \mathbf{g}_{\Gamma^{[i]}})$ $\mathbf{x}^{[n+1]} = H_{\mathbf{s}}(\mathbf{x}^{[n]} + \hat{\mu}^{[n]}\mathbf{g}^{[n]})$ $\Gamma^{[n+1]} = \sup_{\mathbf{p}}(\mathbf{x}^{[n+1]})$ $\mathbf{if} \quad \Gamma^{[n+1]} = \mathbf{r}^{[n]}$ $\mathbf{else} \quad \mathbf{if} \quad \Gamma^{[n+1]} \neq \Gamma^{[n]}$ $\mathbf{b}^{[n]} = (\|\mathbf{x}^{n+1} - \mathbf{x}^n\|_2^2)/(\|\hat{\Phi}_{2n-1}(\mathbf{x}^{n+1} - \mathbf{x}^n)\|_2^2)$ $\mathbf{if} \quad \hat{\mu}^{[n]} \leq (1-c)b^{[n]}$ $\mathbf{x}^{[n+1]} = \mathbf{x}^{[n]}$ $\mathbf{else} \quad \hat{\mu}^{[n]} \sim \hat{\mu}^{[n]}/(k(1-c))$ $\mathbf{x}^{[n+1]} = H_{\mathbf{s}}(\mathbf{x}^{[n]} + \hat{\mu}^{[n]}\mathbf{g}^{[n]})$ $\mathbf{until} \quad \hat{\mu}^{[n]} \leq (1-c)b^{[n]}$ $\Gamma^{[n+1]} = \sup_{\mathbf{p}}(\mathbf{x}^{[n+1]})$

points in a structured manner, we can upper bound the recovery error. In Section 5, we will show that for radio astronomy, we expect this error to be small, given the structure of the measurement matrix.

As introduced earlier, let $\mathbf{x}^{[0]} = 0$ and use the iteration

end for

$$\mathbf{x}^{[n+1]} = H_s(\mathbf{x}^{[n]} + \hat{\mu}^{[n]}Q_b(\mathbf{\Phi})(Q_b(\mathbf{y}) - Q_b(\mathbf{\Phi})\mathbf{x}^{[n]}))$$
(11)

where $Q(\cdot)$ is the quantization function that maps single-precision floating-point values onto a co-domain where each element has b-bits precision.

Quantization Scheme: We analyze a stochastic quantization function denoted with $Q_b(\mathbf{v})$, where $\mathbf{v}=(v_1,v_2,..,v_d)\in\mathbb{R}^d$ is an arbitrary vector and b is the total number of bits used to represent it. \mathbf{v} can then be quantized into $l=2^b$ levels as follows. Let ℓ_i , $i\in\{1,2,...,l-1\}$ denote l equally spaced points on [-1,1] such that $\ell_1=-1$, $\ell_l=+1$ and $\ell_1\leq\ell_2\leq...\leq\ell_l$, also v_j for $j\in\{1,2,...,d\}$ fall into the interval $[\ell_i,\ell_{i+1}]$. Then we assign the probabilities to the nearest levels as

It follows that the quantization operation $Q(\cdot)$ is unbiased, i.e., $\mathbb{E}[Q_b(\mathbf{v})] = \mathbf{v}$. Also, let $\hat{\mathbf{v}}$ represent the quantized \mathbf{v} and drop $Q_b(\cdot)$ to simplify notational burden. The detailed steps of the algorithm are given in Algorithm 1.

Deterministic Quantization: A slightly more efficient compression scheme is via deterministic quantization, i.e., quantize the number $v_j \in [\ell_i, \ell_{i+1}]$ directly to the nearest value, either ℓ_i or ℓ_{i+1} . This quantization scheme will lead to the same error bound and similar empirical result as stochastic quantization. We leave the analysis of this case to the supplementary material.

Convergence: The modified algorithm attains a local minimum of the cost function $\mathbb{E}[\|\hat{\mathbf{y}} - \hat{\mathbf{\Phi}}\mathbf{x}\|_2^2]$ such that $\|\mathbf{x}\|_0 \leq s$. This can be majorized by the following surrogate objective function

$$\mathbb{E}[\|\mu^{0.5}\hat{\mathbf{y}} - \hat{\mathbf{\Phi}}\mathbf{x}\|_{2}^{2} + \|\mathbf{x} - \mathbf{x}^{[n]}\|_{2}^{2} - \|\mu^{0.5}\hat{\mathbf{\Phi}}(\mathbf{x} - \mathbf{x}^{[n]})\|_{2}^{2}]$$

whenever $\|\mu^{0.5}\hat{\Phi}\|_2^2 < 1$. If this condition is met, the minimizer of the above surrogate objective: $\mathbf{x}^{[n+1]}$ ensures that $\mathbb{E}[\|\hat{\mathbf{y}} - \hat{\Phi}\mathbf{x}^{[n+1]}\|_2^2] \leq \mathbb{E}[\|\hat{\mathbf{y}} - \hat{\Phi}\mathbf{x}^{[n]}\|_2^2]$. Moreover, by using the arguments of (Blumensath & Davies, 2008), Eqn. 11 can be shown to minimize the expected cost $\mathbb{E}[\|\hat{\mathbf{y}} - \hat{\Phi}\mathbf{x}\|_2^2]$. For deterministic quantization scheme, Theorem 1 ensures the convergence to a fixed point. We will provide an analysis of the performance guarantee, instead of only convergence.

Conditions on Φ : The restricted isometry property holds for the quantized measurement if

$$\hat{\alpha}_s \le \frac{\|\hat{\mathbf{\Phi}}\mathbf{x}\|_2}{\|\mathbf{x}\|_2} \le \hat{\beta}_s \tag{12}$$

 $\forall \mathbf{x} : \|\mathbf{x}\|_0 \leq s$. Furthermore, the RICs $\hat{\alpha}_s$ and $\hat{\beta}_s$ can be re-scaled accordingly with $\hat{\Phi}$.

4.1. Performance Guarantees

The recovery performance of such algorithms is of our primary interest. The following theorem states the recovery error by explicitly exhibiting the component introduced by the quantization.

Theorem 3. Given a noisy observation $\mathbf{y} = \mathbf{\Phi} \mathbf{x} + \mathbf{e}$ where $\mathbf{y} \in \mathbb{C}^M$, $\mathbf{\Phi} \in \mathbb{C}^{M \times N}$ and $\mathbf{x} \in \mathbb{R}^N$ is an arbitrary vector with $\|\mathbf{x}\|_0 \leq s$. Let $H_s(\mathbf{x}) = \mathbf{x}^s$ with $s \leq M$. Assume $\mathbf{\Phi}$ and $\hat{\mathbf{\Phi}}$ satisfy the non-symmetric RIP with α_s , β_s and $\hat{\alpha}_s$, $\hat{\beta}_s$ where $\gamma_{2s} = \beta_{2s}/\alpha_{2s} - 1 \leq 1/16$ and $\hat{\gamma}_{2s} = \hat{\beta}_{2s}/\hat{\alpha}_{2s} - 1 \leq 1/16$, respectively. If the normalized IHT algorithm is used at low precision we have

$$\mathbb{E}[\|\hat{\mathbf{x}}^{[n+1]} - \mathbf{x}^s\|_2] \le 2^{-n} \|\mathbf{x}^s\|_2 + 10\epsilon_s + 5\epsilon_q \tag{13}$$

with

$$\epsilon_s = \frac{1}{\beta_{2s}} \|\mathbf{e}\|_2 + \left[\|\mathbf{x} - \mathbf{x}^s\|_2 + \frac{\|\mathbf{x} - \mathbf{x}^s\|_1}{\sqrt{s}} \right]$$
 (14)

and

$$\epsilon_q = \frac{\sqrt{M}}{\hat{\beta}_{2s}} \left(\frac{\|\mathbf{x}^s\|_2}{2^{b_{\Phi} - 1}} + \frac{1}{2^{b_{y} - 1}} \right) \tag{15}$$

where b_{Φ} and $b_{\mathbf{y}}$ are the numbers of bits used to represent Φ and \mathbf{y} , respectively.

A natural stopping criterion is $n^* = \lceil \log_2(\|\mathbf{x}^s\|_2/\epsilon_s) \rceil$, where the algorithm computes a successive approximation of \mathbf{x}^s with accuracy

$$\mathbb{E}[\|\mathbf{x}^{[n^*]} - \mathbf{x}^s\|_2] \le 11\epsilon_s + 5\epsilon_q. \tag{16}$$

The error bound above is slightly simplified; our proof in the supplementary material is slightly more delicate. Specifically, the quantization operator introduces only $\frac{5}{\beta 2s} \|\mathbf{e}\|_2$ into $8\epsilon_s$ in Eqn. 8, tighter than the $10\epsilon_s$ in Eqn. 40.

4.2. Discussion and Limitations

We now examine the error bound presented in Theorem 3. Low precision IHT will asymptotically provide a sparse approximation of \mathbf{x} up to the multiples of ϵ_s and ϵ_q involving the noise term \mathbf{e} , the approximation error on how well \mathbf{x} can be represented by a sparse vector \mathbf{x}^s and the noise introduced by the quantization operator. Here we highlight the properties, and stress the limitations of this approach.

Condition on $\hat{\gamma}_{2s}$: In comparison to the unmodified algorithm, the condition under which the performance guarantee holds is stricter in our approach, i.e., $\gamma_{2s}, \hat{\gamma}_{2s} \leq 1/16$ where it was $\gamma_{2s} \leq 1/8$ in Theorem 2. In practice, this can be altered with a suitable transformation of $\hat{\Phi}$ such that $\gamma_{2s}, \hat{\gamma}_{2s} \leq 1/16$ is satisfied. Alternatively, a closer look into the derivation in the supplementary material reveals that there exist finite constants c_1 and c_2 with $c_1 \leq 11$ and $c_2 \leq 5$ such that $\mathbb{E}[\|\mathbf{x}^{n^*} - \mathbf{x}^s\|_2] \leq c_1\epsilon_s + c_2\epsilon_q$ when $\gamma_{2s}, \hat{\gamma}_{2s} \leq 1/8$. For a wide class of problems, an accurate approximation of \mathbf{x}^s can still be recovered after sufficient number of iterations.

Natural limitations on β_{2s} and $\hat{\beta}_{2s}$: In both the low and full precision settings, the measurement matrix Φ is scale-invariant, and rigorous theoretical guarantees are achievable provided its scaling onto sparse vectors is confined in certain intervals, i.e., γ_{2s} , $\hat{\gamma}_{2s} \in [0, 1/16]$. As discussed in Remark 1, even if this condition is met, there still remains a further limitation by the noise \mathbf{e} . That is, the signal-to-noise ratio of $\|\hat{\mathbf{\Phi}}\mathbf{x}\|_2/\|\mathbf{e}\|_2$ will be amplified upon a down-scaling of $\hat{\mathbf{\Phi}}$. Re-scaling \mathbf{y} could accordingly overcome this up to some level.

Further limitations on β_{2s} and $\hat{\beta}_{2s}$ due to quantization: The recovery error bound satisfying Eqn. 40 depends on the error term of full precision IHT: ϵ_s and the quantization error: ϵ_q that are inversely proportional to β_{2s} and $\hat{\beta}_{2s}$, respectively. For sufficiently large values, which compensate for $\|\mathbf{e}\|_2$ and $\sqrt{M}\|\mathbf{x}^s\|_2$, the low precision approach appears competitive with the unmodified algorithm where the recovery error is bounded by $9\epsilon_s$ in Eqn. 8. Furthermore, the scaling-invariant property of the measurement matrix Φ permits us to scale up β_{2s} , hence $\hat{\beta}_{2s}$, by still retaining the strong recovery result similar to that of the full precision algorithm. An arbitrary scaling of Φ has no effect on the condition γ_{2s} , $\hat{\gamma}_{2s} \leq 1/16$. We however have strong theoretical guarantees for recovery if the low precision algorithm operates in a regime where γ_{2s} , $\hat{\gamma}_{2s} \leq 1/16$ holds and ϵ_s and ϵ_q are small.

From the point of view of quantization, re-scaling \mathbf{y} and $\mathbf{\Phi}$ is not necessary. A small factor weightening ϵ_q naturally reduces the quantization error, yet imposes some mild conditions on $\hat{\beta}_{2s}$. Namely, $\hat{\beta}_{2s}$ can not be arbitrary: instead, it is required to satisfy that all entries of $\hat{\mathbf{y}}$ and $\hat{\mathbf{\Phi}}$ are contained in [-1,1].

Comparison to other state-of-art methods: The compressive sensing literature covers a range of algorithms, such as ℓ_1 -minimization, greedy and thresholding-based methods, each with its own trade-offs. In (Blumensath & Davies, 2010), CoSaMP, normalized IHT and ℓ_1 -minimization exhibit similar empirical performance when applied to the problems with dense Gaussian matrices. Moreover, after a simple modification of step size parameter, IHT has became compatible with these powerful methods with similar provable guarantees (Blumensath et al., 2012). In the supplementary material, we show the empirical performance of low precision IHT on such synthetic examples using Gaussian measurement matrices.

4.3. Radio Astronomy Application

In our application, radio interferometers at various locations on the ground record radio waves emitted by the celestial sources over a certain time interval, then store and process these signals to deduce a sky image. Interferometers first estimate the cross-correlation between the time series measurements, called visibilities, and the sky image is estimated by the so-called CLEAN algorithm (Hogbom, 1974). CLEAN is a greedy pursuit technique, deconvolving the inverse Fourier transform of visibilities and forming a sky map by iteratively removing a fraction of the highest peak, convolved with an instrument based point spread function. CLEAN is a simple and easy-to-implement imaging technique. However radio interferometers are also phrased as a CS problem, for example, by (Wiaux et al., 2009; Wenger et al., 2010; Li et al., 2011) because of their recovery success in noisy environments.

Assume the sky is observed by employing L antennas over a stationary time interval where the earth rotation is negligible. Denote the vectorized sky image by $\mathbf{x} \in \mathbb{R}^N$ with $N = r^2$ where r is the resolution of images, i.e., height and width of the image in pixels. We formulate the interferometer pipeline as a compressive sensing problem such that $\mathbf{y} = \mathbf{\Phi}\mathbf{x} + \mathbf{e}$ where $\mathbf{\Phi} \in \mathbb{C}^{M \times N}$ is the measurement matrix with complex entries as a function of inner product between antenna and pixel locations, $\mathbf{y} \in \mathbb{C}^M$ is the visibilities where $M = L^2$, and $\mathbf{e} \in \mathbb{C}^M$ is the noise vector. For more background on the radio interferometer pipeline and formation of $\mathbf{\Phi}$, please see Section 3 of the supplementary material.

Why iterative hard thresholding? According to our formulation, the measurement vector \mathbf{y} represents the cross-correlations between the antenna measurements: the visibilities. The naive method to map from \mathbf{y} to a vectorized sky image \mathbf{x} is the Fourier inversion followed by the CLEAN algorithm. Alternatively, A(W)-projection algorithm initially makes corrections on the visibilities then deduces a sky image (Bhatganar et al., 2008). Still, forming a sky map using the non-uniform samples of visibility functions recorded by finite number of antennas is naturally inaccurate. Furthermore, the thermal noise introduced by the electronic instruments embedded in the RF antenna receivers heavily corrupt the weak incoming signal, and therefore pose a further challenge for these imaging algorithms. To date, the current techniques revolve around carrying out noise reduction by collecting lots of data, so that the noise can be circumvented. The choice of IHT can be justified by its robustness to noise. We demonstrate this in detail, via further experiments in the supplementary material, where we show that the baseline CLEAN approach often resolves noise artefacts as actual sky sources.

We refine our error bound for the radio astronomy scenario:

Corollary 1. Let σ_n^2 is the variance of noise introduced by a single antenna. By Theorem 3, if $\gamma_{2s}, \hat{\gamma}_{2s} \leq 1/16$, the low precision iterative hard thresholding recovers the sky image \mathbf{x}^s with accuracy

$$\mathbb{E}[\|\mathbf{x}^{n+1} - \mathbf{x}^s\|_2] \le 2^{-n} \|\mathbf{x}^s\|_2 + 10(\frac{\sqrt{L}}{\beta_{2s}} \sigma_n + \frac{L}{\hat{\beta}_{2s}} \epsilon_{\text{sky}})$$

$$\tag{17}$$

where $\epsilon_{\rm sky} = \|\mathbf{x}^s\|_2 / 2^{b_{\Phi}} + 1/2^{b_{y}}$.

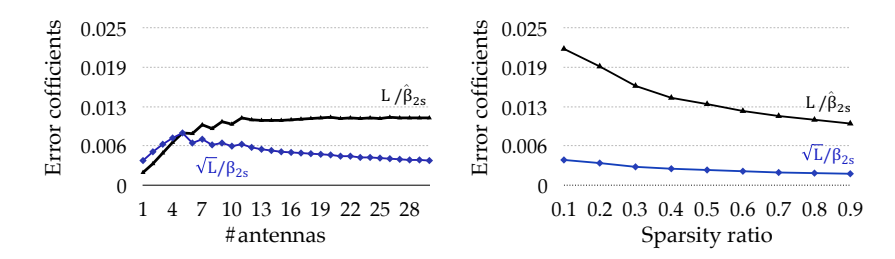


Fig 3. Monitoring the error coefficients: \sqrt{L}/β_{2s} and $L/\hat{\beta}_{2s}$ that scale σ_n and $\|\mathbf{x}^s\|_2$ that appear in the recovery error bound, respectively. Sparsity ratio stands for s/M. The numerical value of coefficients guarantees that $\|\mathbf{x}^{[n+1]} - \mathbf{x}^s\|_2/\|\mathbf{x}^s\|_2$ is sufficiently small regardless of the number of bits to represent Φ .

Discussion: LOFAR and Beyond. Corollary 1 shows that the sky image can be recovered with high accuracy when certain conditions hold: β_{2s} and $\hat{\beta}_{2s}$ are sufficiently large, γ_{2s} and $\hat{\gamma}_{2s}$ are sufficiently small. Do these conditions hold for a real telescope? We now analyze it for one station of the LOFAR telescope, and discuss it further for radio interferometers in general.

Recall from Theorem 3 the two conditions ensuring performance guarantees: (a) γ_{2s} , $\hat{\gamma}_{2s} \leq 1/16$, (b) $L/\hat{\beta}_{2s}$ must be large to minimize quantization error ϵ_q . Fortunately, in the radio interferometry application, the image grid we initially form as well as scale-invariant property of normalized IHT yield us the control over γ_{2s} , $\hat{\gamma}_{2s}$ and β_{2s} , $\hat{\beta}_{2s}$, respectively, through a pre-processing of Φ . Analytic derivations of these parameters are possible in theory, but intractable due to amount of nonlinear operations contained in the formulation of Φ .

In Fig. 3, for station CS302 of LOFAR, we first form the image grid and compute and adjust Φ , $\hat{\Phi}$ such that α_{2s} , $\hat{\alpha}_{2s} \leq 1/16$ holds. We refer the reader to the supplementary material for more details. Then we numerically compute the scaling factors of errors σ_n and ϵ_{sky} : \sqrt{L}/β_{2s} and $L/\hat{\beta}_{2s}$, respectively. Theorem 3 states that the recovery error is induced by two terms: \sqrt{L}/β_{2s} and $L/\hat{\beta}_{2s}$. Therefore, we investigate these scaling over various antenna numbers and sparsity level. The results suggest that 2-bits IHT has a negligible quantization error when applied radio interferometry imaging problem.

4.4. FPGA Implementation Details

Field-Programmable Gate Arrays (FPGA) are an alternative to commonly used Graphics Processing Units (GPU) for accelerated processing of compute intensive machine learning workloads. The custom logic fabric of an FPGA enables the design of specialized compute units, which is very advantageous when working on extremely low-precision and irregular numeric formats, such as 2 bit numbers. Thanks to the microarchitectural flexibility advantage, it is possible to achieve near linear speed-up when lowering the precision of data that is read from the memory. This has been shown recently for stochastic gradient descent (SGD) when training linear models (Zhang et al., 2017; Kara et al., 2017). In this work, we use the open-source FPGA implementation from the mentioned works and modify it to perform IHT.

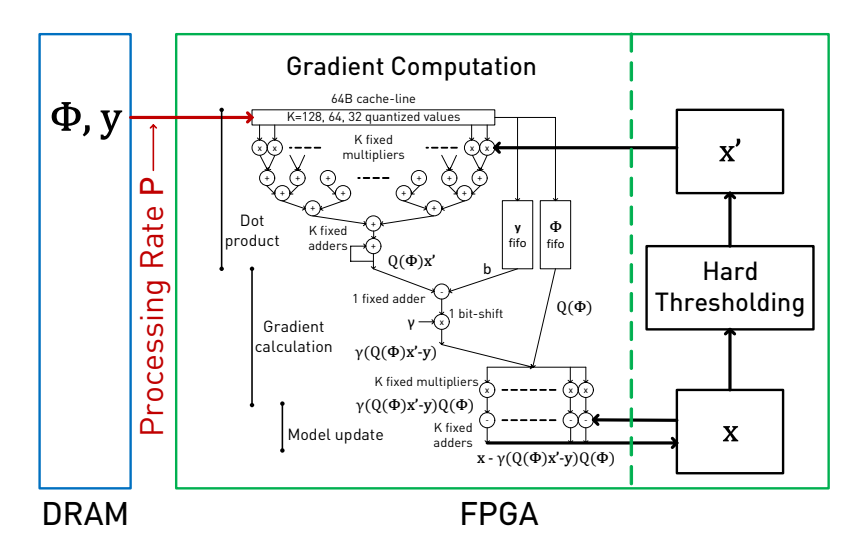


Fig 4. IHT on an FPGA-based system.

In terms of the computation, we need to modify two parts of the design to convert it from performing SGD to IHT: 1) Instead of updating the model after a mini-batch count is reached, we update it after all samples are processed and the true gradient is available. 2) After each epoch, we perform a binary search on the updated model to find the threshold value satisfying that only top S values are larger than the threshold.

Performance analysis The gradient computation unit as shown in Fig. 4 reads the measurement matrix $\mathbf{\Phi}$ and the measurements \mathbf{y} from main memory and keeps \mathbf{x} in on-chip memory. We note that transferring $\mathbf{\Phi}$ from main memory will be necessary in most practical settings, where the matrix $\mathbf{\Phi}$ is too large to fit onto the FPGA. The FPGA is able to process data from memory at a rate of $\mathbf{P} = 12.8\,GB/s$. Thus, performance will be bound on this rate \mathbf{P} for processing $\mathbf{\Phi}$ and \mathbf{y} , which becomes the system bottleneck. The time for each iteration is given by $T = size(\mathbf{\Phi})/\mathbf{P}$, since $size(\mathbf{y}) \ll size(\mathbf{\Phi})$. We can achieve significant speed-up by quantizing $\mathbf{\Phi}$, simply because we reduce the amount of data to be transferred: more entries arrive with each transfer from main memory. The processing rate \mathbf{P} can be kept constant on an FPGA, because we can adapt the gradient computation unit's microarchitecture and increase its internal parallelism to handle more values per incoming line.

Computing Φ on the fly The above analysis focuses on the case when Φ is stored in main memory, in which case quantization helps to reduce the amount of data transferred between the main memory and FPGA. In some applications, Φ can be calculated on the fly, inside the FPGA. Also in this case, quantization can help achieve better performance. The reason why quantizing Φ helps, even if it can be calculated on the fly, is that a quantized Φ saves many crucial resources (e.g., multipliers) that are limited on an FPGA. These resource savings are very important in achieving a higher internal parallelism, for instance, to speed up the computation of $\Phi \times \mathbf{x}$. For example, it has been shown by (Kara et al., 2017) that to go from a 64-value dot product to 128-value dot product on an FPGA, it is necessary to

lower the precision of one side of the dot product to 2-bits.

5. Experimental Results

We assess the empirical performance of our approach using the radio interferometer measurements from a real telescope: the LOw Frequency ARray (LOFAR). We first demonstrate that the accuracy achieved in the low precision setting is comparable with high precision IHT and other state-of-art methods; we then show the speed-up on FPGA.

5.1. Accuracy of Sky Recovery

We recover the full sky image of the resolution 256×256 pixels ($\mathbf{x} \in \mathbb{R}^{65,536}$ in vectorized form) by employing 30 low-band antennas of LOFAR CS302 station that operates in 15-80 MHz frequency band where the sky is populated with 30 strong sources, that is, $\mathbf{y} \in \mathbb{C}^{900}$, $\hat{\mathbf{\Phi}} \in \mathbb{C}^{900 \times 65,536}$. The signal-to-noise ratio is 0 dB at the antenna level, i.e., $10 \log_{10}(\|\mathbf{\Phi}\mathbf{x}\|_2^2/\|\mathbf{e}\|_2^2) = 0$ dB.

Improving least square estimates Fig. 1 provides an example of sky recoveries: (a) ground truth estimated over 12 hours of observation, (b) a least square estimate of underlying sky (or dirty image in the nomenclature of radio astronomy), (c) 32 bit and (d) 2&8 bit (normalized) IHT which uses 2 bits for the measurement matrix and 8 bits for the observation. This experiment indicates that low precision IHT captures the sky sources successfully even when only 2 bit are used to compress Φ . Thus, we can drastically reduce the data precision yet still estimate the sky precisely.

This strong empirical performance is not completely surprising. Mathematically, the measurement matrix we formed here reflects the phase relations, as induced by the antenna locations. That is, each time a bit $r_{m,n}$ or $c_{m,n}$ flips its sign where $\hat{\Phi}_{m,n} = r_{m,n} + jc_{m,n}$, m = 1, 2, ..., M and n = 1, 2, ..., N, we approximately know the change in horizontal and vertical directions on the ground, preserving the phase information required for interferometric imaging even at very low precision.

Comparison to state-of-art methods We compare low precision IHT to full precision IHT, CoSaMP and an ℓ_1 -based approach in terms of their capability to recover sparse signals. For this particular formulation of the interferometric imaging problem, they can iteratively build up an estimate of the sky map \mathbf{x} . To avoid bias towards any algorithm, we optimized each algorithm independently.

We first evaluate algorithms through two metrics: (1) the recovery error and (2) exact recovery, that is, the ratio of support that is successfully recovered. In radio interferometry, however, it is customary to use number of true celestial sources resolved in the recovered image as a performance metric, i.e., true-positive findings. That is, the performance of the algorithms is no longer described by its ability to recover support entirely but the sky objects, which possess higher error tolerance. We demonstrate in Fig. 5 that IHT performs as well as its alternatives and compatible to ℓ_1 -minimization in terms of its exact recovery performance. Empirical results suggest that the celestial sources can still be recovered when dramatically quantizing Φ .

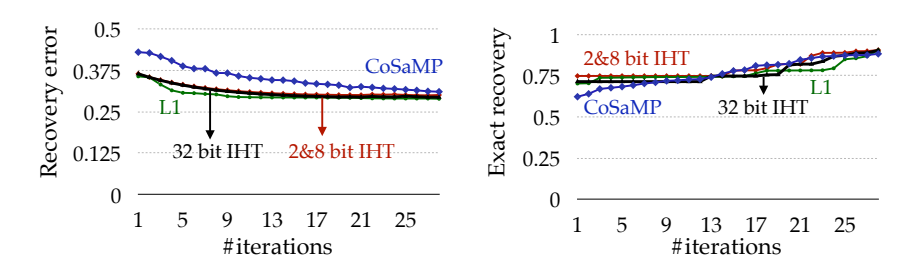


Fig 5. Comparison of recovery error and exact recovery (support): 288 bit IHT vs. 32 bit IHT, CoSaMP, & ℓ_1 .

Discussion: This experiment is informative merely on the accuracy of the results obtained implementing these alternative algorithms. A fair comparison involves the analysis of different properties such as speed and storage requirements, flexibility and ease of implementation. IHT is known to outperform CoSaMP when Φ has similar entries in magnitude (Blumensath et al., 2012), which is confirmed by our experiments. Empirical evidence further suggests that IHT performs nearly as well as the ℓ_1 -based approach. The low precision approach has similar recovery performance as high precision IHT, as shown in Fig. 5.

5.2. Speed-up on FPGA

We demonstrate the speed up for performing IHT on the FPGA-based system in Fig. 6. For the time spent per iteration, we see that quantization, and the resulting compression of the measurement matrix Φ leads to near linear speed up for recovering the support vector. As previously studied in the performance analysis part in Section 4.4, all variants (full precision to lowest precision) of IHT on FPGA can consume Φ at the same rate, and therefore the runtime of IHT depends linearly on the size of Φ , leading to linear speed ups that we observe in the experiments.

In terms of end-to-end performance, we measure the time for each precision level needs to reach support recovery ratio 90% and calculate the speedup. The 2&8-bit IHT variant reaches the same support recovery ratio $9.19 \times$ faster.

6. Discussion

We investigated the applicability of low precision schemes to sparse signal recovery problems, and introduced a low-precision NIHT variant, with theoretical guarantees and good practical performance, both in terms of accuracy and recovery time. The radio astronomy application validated our claims, and showed that the heuristic and rigorous arguments are in agreement with experiments. The results bear out that our approach offers similar accuracy with the high precision IHT even with far less precision of data points. Further, we showed that even when using 2 bits to represent data, the accuracy of sparse approximations can still be preserved, and significant practical speed up can be achieved.

There are several questions for future work. In particular: Can we devise algorithms which work with end-to-end low precision data representation? Can we extend these techniques to

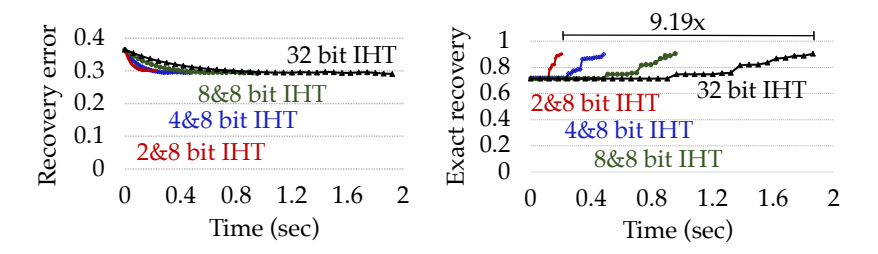


Fig 6. Speed-up of low precision IHT on FPGA. 288 bit IHT provides 9.19× speedup versus full-precision.

other greedy recovery algorithms, and other sparse recovery frameworks?

Proofs

We begin by introducing our notation.

- 1. $\mathbf{y} = \mathbf{\Phi}\mathbf{x} + \mathbf{e} = \mathbf{\Phi}\mathbf{x}^s + \mathbf{\Phi}(\mathbf{x} \mathbf{x}^s) + \mathbf{e}$,
- 2. $\varepsilon = \Phi(\mathbf{x} \mathbf{x}^s) + \mathbf{e}$, hence $\mathbf{y} = \Phi \mathbf{x}^s + \varepsilon$,
- 3. $\epsilon_{\mathbf{y}} = Q(\mathbf{y}, b) \mathbf{y}$,
- 4. $\Gamma^{[n]} = \sup\{\mathbf{x}^{[n]}\}, \ \hat{\Gamma}^{[n]} = \sup\{\hat{\mathbf{x}}^{[n]}\} \text{ and } \Gamma^s = \sup\{\mathbf{x}^s\},$ 5. $B^{[n]} = \Gamma^{[n]} \cup \Gamma^s \text{ and } B^{[n]} = \hat{\Gamma}^{[n]} \cup \Gamma^s,$
- 6. $\mathbf{a}^{[n+1]} = \hat{\mathbf{x}}^{[n]} + \mu^{[n]} \mathbf{\Phi}^{\dagger} (\mathbf{y} \mathbf{\Phi} \hat{\mathbf{x}}^{[n]}) \text{ and } \hat{\mathbf{a}}^{[n+1]} = \hat{\mathbf{x}}^{[n]} + \hat{\mu}^{[n]} Q_1 (\mathbf{\Phi})^{\dagger} (\mathbf{y} Q_2 (\mathbf{\Phi}) \hat{\mathbf{x}}^{[n]}),$ 7. $\mathbf{x}^{[n+1]} = H_s(\mathbf{a}^{[n+1]}) \text{ and } \hat{\mathbf{x}}^{[n+1]} = H_s(\hat{\mathbf{a}}^{[n+1]}),$
- 8. $\mathbf{r}^{[n]} = \hat{\mathbf{x}}^{[n]} \mathbf{x}^s$.

Assume Φ satisfies the non-symmetric Restricted Isometry Property

$$\alpha_s \le \frac{\|\mathbf{\Phi}\mathbf{x}\|_2}{\|\mathbf{x}\|_2} \le \beta_s \tag{18}$$

for all $\mathbf{x}: \|\mathbf{x}\|_0 \leq s$, where $\alpha_s \in \mathbb{R}$ and $\beta_s \in \mathbb{R}$ are the lowest and largest singular value of Φ such that $0 < \alpha_s \le \beta_s$, the so-called restricted isometric constants. Inherent from its definition, the restricted isometry holds for the quantized measurement matrix denoted by $Q(\mathbf{\Phi}, b_m)$ such that

$$\hat{\alpha}_s \le \frac{\|Q(\mathbf{\Phi}, b_m)\mathbf{x}\|_2}{\|\mathbf{x}\|_2} \le \hat{\beta}_s \tag{19}$$

where $\hat{\alpha}_s$ and $\hat{\beta}_s$ are associated restricted isometry constants. For simplicity, we drop b_m , and use $Q(\Phi)$ instead. Also, let $\gamma_s = \beta_s/\alpha_s - 1$ and $\hat{\gamma}_s = \hat{\beta}_s/\hat{\alpha}_s - 1$.

Remark 2. The adaptive setting of step size parameter $\mu^{[n]}$ and $\hat{\mu}^{[n]}$ in normalized IHT is shown to satisfy

$$1/\beta_{2s}^2 \le \mu^{[n]} \le 1/\alpha_{2s}^2,\tag{20}$$

$$1/\hat{\beta}_{2s}^2 \le \hat{\mu}^{[n]} \le 1/\hat{\alpha}_{2s}^2. \tag{21}$$

We will start by stating the following fundamental results.

Lemma 1. (Blumensath & Davies, 2010) If Φ satisfies the restricted isometry property, then for $|\Gamma| \leq 2s$

$$\|\mathbf{\Phi}_{\Gamma}^T \mathbf{x}\|_2 \le \beta_{2s} \|\mathbf{x}\|_2,\tag{22}$$

$$\|\mu^{[n]} \mathbf{\Phi}_{\Gamma}^T \mathbf{\Phi}_{\Gamma} \mathbf{x}_{\Gamma}\|_2 \le (\gamma_{2s} + 1) \|\mathbf{x}_{\Gamma}\|_2, \tag{23}$$

$$\|(\mathbf{I} - \mu^{[n]} \mathbf{\Phi}_{\Gamma}^T \mathbf{\Phi}_{\Gamma}) \mathbf{x}_{\Gamma}\|_2 \le \gamma_{2s} \|\mathbf{x}_{\Gamma}\|_2, \tag{24}$$

$$\|\mu^{[n]} \mathbf{\Phi}_{\Upsilon}^T \mathbf{\Phi}_{\Lambda} \mathbf{x}_{\Lambda}\|_2 \le \gamma_{2s} \|\mathbf{x}_{\Lambda}\|_2, \tag{25}$$

where Υ and Λ are two disjoint sets (i.e., $\Upsilon \cap \Lambda = \emptyset$) such that $|\Upsilon \cup \Lambda| \leq 2s$.

Clearly, similar results hold for $Q(\Phi)$ such that

$$\|Q(\mathbf{\Phi})^T_{\Gamma}\mathbf{x}\|_2 \le \hat{\beta}_{2s}\|\mathbf{x}\|_2,\tag{26}$$

$$\|\mu^{[n]}Q(\mathbf{\Phi})_{\Gamma}^{T}Q(\mathbf{\Phi})_{\Gamma}\mathbf{x}_{\Gamma}\|_{2} \le (\hat{\gamma}_{2s} + 1)\|\mathbf{x}_{\Gamma}\|_{2},$$
 (27)

$$\|(\mathbf{I} - \mu^{[n]} Q(\mathbf{\Phi})_{\Gamma}^T Q(\mathbf{\Phi})_{\Gamma}) \mathbf{x}_{\Gamma}\|_2 \le \hat{\gamma}_{2s} \|\mathbf{x}_{\Gamma}\|_2, \tag{28}$$

$$\|\mu^{[n]}Q(\mathbf{\Phi})_{\Upsilon}^TQ(\mathbf{\Phi})_{\Lambda}\mathbf{x}_{\Lambda}\|_2 \le \hat{\gamma}_{2s}\|\mathbf{x}_{\Lambda}\|_2. \tag{29}$$

Lemma 2. (Blumensath & Davies, 2010) For any \mathbf{x} , let \mathbf{x}^s be the best s-term approximation to \mathbf{x} and Υ be a set with at most s elements. Then

$$\|\mu^{[n]} \mathbf{\Phi}_{\Upsilon}^T \mathbf{\Phi}(\mathbf{x} - \mathbf{x}^s)\|_2 \le (1 + \gamma_{2s}) [\|\mathbf{x} - \mathbf{x}^s\|_2] + \frac{\|\mathbf{x} - \mathbf{x}^s\|_2}{\sqrt{s}}].$$
 (30)

Based on the properties above, the restricted isometry, which we will require repeatedly throughout the proof, has several other consequences, summarized as follows.

Corollary 2. Suppose $Q(\Phi)$ satisfies restricted isometry property in Eqn. 19. Then

$$\|(\mu^{[n]}\boldsymbol{\Phi}_{\Gamma}^{T} - \hat{\mu}^{[n]}Q(\boldsymbol{\Phi})_{\Gamma}^{T})\mathbf{x}_{\Gamma}\|_{2} \leq \max((1 + \gamma_{2s})/\beta_{2s} - 1/\hat{\beta}_{2s}, (1 + \hat{\gamma}_{2s})/\hat{\beta}_{2s} - 1/\beta_{2s})\|\mathbf{x}_{\Gamma}\|_{2}, (31)$$

$$\|(\mu^{[n]}\boldsymbol{\Phi}_{\Gamma}^T\boldsymbol{\Phi}_{\Gamma} - \mu^{[n]}Q_1(\boldsymbol{\Phi})_{\Gamma}^TQ_2(\boldsymbol{\Phi})_{\Gamma})\mathbf{x}_{\Gamma}\|_2 \le \max(\gamma_{2s}, \hat{\gamma}_{2s})\|\mathbf{x}_{\Gamma}\|_2, \tag{32}$$

$$\|(\mu^{[n]}\boldsymbol{\Phi}_{\Upsilon}^T\boldsymbol{\Phi}_{\Lambda} - \mu^{[n]}Q_1(\boldsymbol{\Phi})_{\Upsilon}^TQ_2(\boldsymbol{\Phi})_{\Lambda})\mathbf{x}_{\Lambda}\|_2 \le \max(\gamma_{2s}, \hat{\gamma}_{2s})\|\mathbf{x}_{\Lambda}\|_2. \tag{33}$$

Proof. As a simple consequence of restricted isometry property, the singular values of Φ_{Γ} lie between α_{2s} and β_{2s} . Reminding that $\mu^{[n]}$ is chosen to satisfy $1/\beta_{2s}^2 \leq \mu^{[n]} \leq 1/\alpha_{2s}^2$ we have

$$1/\beta_{2s} \|\mathbf{x}_{\Gamma}\|_{2} \leq \|\mu^{[n]} \mathbf{\Phi}_{\Gamma} \mathbf{x}_{\Gamma}\|_{2} \leq (1 + \gamma_{2s})/\beta_{2s} \|\mathbf{x}_{\Gamma}\|_{2}.$$
(34)

It similarly holds for $Q(\mathbf{\Phi})$:

$$1/\hat{\beta}_{2s} \|\mathbf{x}_{\Gamma}\|_{2} \leq \|\hat{\mu}^{[n]} Q(\mathbf{\Phi})_{\Gamma} \mathbf{x}_{\Gamma}\|_{2} \leq (1 + \hat{\gamma}_{2s})/\hat{\beta}_{2s} \|\mathbf{x}_{\Gamma}\|_{2}. \tag{35}$$

Singular values of $\mu^{[n]} \Phi_{\Gamma}^T - \hat{\mu}^{[n]} Q(\Phi)_{\Gamma}^T$ therefore fall in the interval $[(1 + \hat{\gamma}_{2s})/\hat{\beta}_{2s} - 1/\hat{\beta}_{2s}, (1 + \gamma_{2s})/\beta_{2s} - 1/\hat{\beta}_{2s}]$. Eqn. 31 then trivially holds.

Using restricted isometry property in Eqn. 18 & 19 over 2s-sparse vectors, similar argument holds for Eqn. 32, that is, the singular values of Φ_{Γ} and $Q(\Phi)_{\Gamma}$ fall into $[1, 1 + \gamma_{2s}]$

and $[1, 1+\hat{\gamma}_{2s}]$, respectively. Then $\|\mu^{[n]} \mathbf{\Phi}_{\Gamma}^T \mathbf{\Phi}_{\Gamma} - \mu^{[n]} Q_1(\mathbf{\Phi})_{\Gamma}^T Q_2(\mathbf{\Phi})_{\Gamma}\|_2$ is bounded above by the term $\max((1+\hat{\gamma}_{2s})-1, (1+\gamma_{2s})-1)$, which proves Eqn. 32.

Eqn. 33 is a consequence of the fact that $-\mu^{[n]} \Phi_{\Upsilon}^T \Phi_{\Lambda}$ is a submatrix of $I - \mu^{[n]} \Phi_{\Upsilon \cup \Lambda}^T \Phi_{\Upsilon \cup \Lambda}$, which in turn implies that $\|\mu^{[n]} \Phi_{\Upsilon}^T \Phi_{\Lambda}\|_2 \leq \|I - \mu^{[n]} \Phi_{\Upsilon \cup \Lambda}^T \Phi_{\Upsilon \cup \Lambda}\|_2$, (i.e., spectral norm of a submatrix is bounded by the norm of its full matrix). Using Eqn. 23, the eigenvalues of $\mu^{[n]} \Phi_{\Upsilon}^T \Phi_{\Lambda}$ can be shown to be in $[0, \gamma_{2s}]$, and in parallel, $\hat{\mu}^{[n]} Q(\Phi)_{\Upsilon}^T Q(\Phi)_{\Lambda}$ in $[0, \hat{\gamma}_{2s}]$. The difference $I - \mu^{[n]} \Phi_{\Upsilon \cup \Lambda}^T \Phi_{\Upsilon \cup \Lambda}$ then have eigenvalues no larger than $\max(\gamma_{2s}, \hat{\gamma}_{2s})$.

Lemma 3. Let $Q(\cdot, b) : \mathbb{R}^M \times \mathbb{Z}^+ \to \mathbb{R}^d$ denote quantization operator described in the paper. For any $\mathbf{v} \in \mathbb{R}^d$, the norm of quantization error can be bounded by

$$\mathbb{E}[\|Q(\mathbf{v},b) - \hat{\mathbf{v}}\|_2] \le \frac{\sqrt{M}}{2^{b-1}}$$
(36)

where $\hat{\mathbf{v}}$ is a scaled version of \mathbf{v} so that every component is normalized to [-1,1].

Remark 3. For efficient fixed-point computation on Field Programmable Gate Array, we need an odd number of quantization levels, and therefore total number of levels for b bit quantization is $2^{b-1}+1$. That is, the interval between two consecutive levels is 2^{b-1} provided the values are confined in the interval [-1,1] a priori.

Proof. Using Jensen's inequality we can easily show that

$$\mathbb{E}[\|Q(\hat{\mathbf{v}},b) - \hat{\mathbf{v}}\|_{2}] = \mathbb{E}\left[\sqrt{\|Q(\hat{\mathbf{v}},b) - \hat{\mathbf{v}}\|_{2}^{2}}\right]$$

$$\leq \sqrt{\mathbb{E}[\|Q(\hat{\mathbf{v}},b) - \hat{\mathbf{v}}\|_{2}^{2}]}$$

$$\leq \sqrt{\sum_{i=1}^{M} \mathbb{E}[(Q(\hat{\mathbf{v}},b)_{i} - \hat{v}_{i})^{2}]}$$

$$\leq \sqrt{\sum_{i=1}^{M} \mathbb{P}(Q(\hat{\mathbf{v}},b)_{i} = \ell_{j})(\hat{v}_{i} - \ell_{j})^{2} + \mathbb{P}(Q(\hat{\mathbf{v}},b)_{i} = \ell_{j+1})(\ell_{j+1} - \hat{v}_{i})^{2}}.$$
(37)

Our quantization scheme uses a stochastic approach such that $\mathbb{P}(Q(\hat{\mathbf{v}},b)_i=\ell_j)=\frac{\ell_{j+1}-\hat{v}_i}{\ell_{j+1}-\ell_j}$, and hence $\mathbb{P}(Q(\hat{\mathbf{v}},b)_i=\ell_{j+1})=1-\frac{\ell_{j+1}-\hat{v}_i}{\ell_{j+1}-\ell_j}$. Substituting these into Eqn. 37 we have

$$\mathbb{E}[\|Q(\hat{\mathbf{v}},b) - \hat{\mathbf{v}}\|_2] \le \sqrt{\sum_{i=1}^n (l_{j+1} - Q(\hat{\mathbf{v}},b)_i)(Q(\hat{\mathbf{v}},b)_i - \ell_j)}.$$
 (38)

It can easily be seen that $(l_{j+1}-Q(\hat{\mathbf{v}},b)_i)(Q(\hat{\mathbf{v}},b)_i-\ell_j)$ is maximized when $Q(\hat{\mathbf{v}},b)_i)=\frac{\ell_{j+1}-\ell_j}{2}$, moreover quantization function implies that $\ell_{j+1}-\ell_j=\frac{1-(-1)}{l}=\frac{1}{2^{b-2}}$

$$\mathbb{E}[\|Q(\hat{\mathbf{v}},b) - \hat{\mathbf{v}}\|_{2}] \leq \sqrt{\sum_{i=1}^{M} \frac{(\ell_{j+1} - \ell_{j})^{2}}{4}}$$

$$\leq \frac{\sqrt{M}(\ell_{j+1} - \ell_{j})}{2}$$

$$\leq \frac{\sqrt{M}}{2^{b-1}}.$$
(39)

Proof of Theorem 3

The recovery error can be split into two parts by using triangle inequality

$$\mathbb{E}[\|\hat{\mathbf{x}}^{[n+1]} - \mathbf{x}^{s}\|_{2}|\hat{\mathbf{x}}^{[n]}] = \mathbb{E}[\|\hat{\mathbf{x}}_{B^{[n+1]}}^{[n+1]} - \mathbf{x}_{B^{[n+1]}}^{s}\|_{2}|\hat{\mathbf{x}}^{[n]}] \\
\leq \mathbb{E}[\|\hat{\mathbf{x}}_{B^{[n+1]}}^{[n+1]} - \hat{\mathbf{a}}_{B^{[n+1]}}^{[n+1]}\|_{2}|\hat{\mathbf{x}}^{[n]}] + \mathbb{E}[\|\hat{\mathbf{a}}_{B^{[n+1]}}^{[n+1]} - \mathbf{x}_{B^{[n+1]}}^{s}\|_{2}|\hat{\mathbf{x}}^{[n]}]. \tag{40}$$

where the equality follows from that $\hat{\mathbf{x}}^{[n+1]} - \mathbf{x}^s$ is supported over the set $B^{[n+1]} = \hat{\Gamma}^{[n+1]} \cup \Gamma^s$. Recall that $\hat{\mathbf{x}}_{B^{[n+1]}}^{[n+1]}$ is a better s-term approximation to $\hat{\mathbf{a}}_{B^{[n+1]}}^{[n+1]}$ than $\mathbf{x}_{B^{[n+1]}}^s$ (i.e., $\|\hat{\mathbf{x}}^{[n+1]} - \hat{\mathbf{a}}_{B^{[n+1]}}^{[n+1]}\|_2 \leq \|\hat{\mathbf{a}}_{B^{[n+1]}}^{[n+1]} - \mathbf{x}^s\|_2$). Then

$$\mathbb{E}[\|\hat{\mathbf{x}}^{[n+1]} - \mathbf{x}^s\|_2 |\hat{\mathbf{x}}^{[n]}] \le 2\mathbb{E}[\|\hat{\mathbf{a}}_{B^{[n+1]}}^{[n+1]} - \mathbf{x}_{B^{[n+1]}}^s\|_2 |\hat{\mathbf{x}}^{[n]}]. \tag{41}$$

Using triangle inequality, we further have

$$\mathbb{E}[\|\hat{\mathbf{x}}^{[n+1]} - \mathbf{x}^s\|_2 |\hat{\mathbf{x}}^{[n]}] \le 2 \left[\mathbb{E}[\|\hat{\mathbf{a}}_{B^{[n+1]}}^{[n+1]} - \mathbf{a}_{B^{[n+1]}}^{[n+1]}\|_2 + \|\mathbf{a}_{B^{[n+1]}}^{[n+1]} - \mathbf{x}_{B^{[n+1]}}^s \|_2 |\hat{\mathbf{x}}^{[n]}] \right]$$
(42)

We now continue with the analysis referring to two terms on the right hand side of Eqn. 42 separately.

(a) Expanding $\hat{\mathbf{a}}_{B^{[n+1]}}^{[n+1]}$ and $\mathbf{a}_{B^{[n+1]}}^{[n+1]}$ we have

$$\mathbb{E}[\|\hat{\mathbf{a}}_{B^{[n+1]}}^{[n+1]} - \mathbf{a}_{B^{[n+1]}}^{[n+1]}\|_{2}|\hat{\mathbf{x}}^{[n]}] \\
= \mathbb{E}[\|\hat{\mu}^{[n]}Q_{1}(\mathbf{\Phi})_{B^{[n+1]}}^{T}(Q_{y}(\mathbf{y}) - Q_{2}(\mathbf{\Phi})\hat{\mathbf{x}}^{[n]}) - \mu^{[n]}\mathbf{\Phi}_{B^{[n+1]}}^{T}(\mathbf{y} - \mathbf{\Phi}\hat{\mathbf{x}}^{[n]})\|_{2}|\hat{\mathbf{x}}^{[n]}] \\
= \mathbb{E}[\|\hat{\mu}^{[n]}Q_{1}(\mathbf{\Phi})_{B^{[n+1]}}^{T}(\mathbf{\Phi}\mathbf{x}^{s} + \varepsilon + \epsilon_{y} - Q_{2}(\mathbf{\Phi})\hat{\mathbf{x}}^{[n]}) - \mu^{[n]}\mathbf{\Phi}_{B^{[n+1]}}^{T}(\mathbf{\Phi}\mathbf{x}^{s} + \varepsilon - \mathbf{\Phi}\hat{\mathbf{x}}^{[n]})\|_{2}|\hat{\mathbf{x}}^{[n]}] \\
= \mathbb{E}[\|\hat{\mu}^{[n]}Q_{1}(\mathbf{\Phi})_{B^{[n+1]}}^{T}(-Q_{2}(\mathbf{\Phi})\mathbf{r}^{[n]} + \varepsilon + \epsilon_{y} + (\mathbf{\Phi} - Q_{2}(\mathbf{\Phi}))\mathbf{x}^{s}) + \mu^{[n]}\mathbf{\Phi}_{B^{[n+1]}}^{T}(\mathbf{\Phi}\mathbf{r}^{[n]} - \varepsilon)\|_{2}|\hat{\mathbf{x}}^{[n]}] \\
\leq \|(\mu^{[n]}\mathbf{\Phi}_{B^{[n+1]}}^{T}\mathbf{\Phi} - \hat{\mu}^{[n]}Q_{1}(\mathbf{\Phi})_{B^{[n+1]}}^{T}Q_{2}(\mathbf{\Phi}))\mathbf{r}^{[n]}\|_{2} \\
+ \|(\mu^{[n]}\mathbf{\Phi}_{B^{[n+1]}}^{T} - \hat{\mu}^{[n]}Q_{1}(\mathbf{\Phi})_{B^{[n+1]}}^{T})\varepsilon\|_{2} \\
+ \mathbb{E}[\|\hat{\mu}^{[n]}Q_{1}(\mathbf{\Phi})_{B^{[n+1]}}^{T}\epsilon_{y}\|_{2}] \\
+ \mathbb{E}[\|\hat{\mu}^{[n]}Q_{1}(\mathbf{\Phi})_{B^{[n+1]}}^{T}(\mathbf{\Phi} - Q_{2}(\mathbf{\Phi}))\mathbf{x}^{s}\|_{2}]. \tag{43}$$

where we used the expansion $\mathbf{r}^{[n]} = \hat{\mathbf{x}}^{[n]} - \mathbf{x}^s$. We further derive the terms governing the above expression in (a.1), (a.2), (a.3) and (a.4).

(a.1) Since $\mathbf{r}^{[n]}$ is supported over $B^{[n]}$, we clearly have

$$\begin{split} &\| \left(\mu^{[n]} \mathbf{\Phi}_{B^{[n+1]}}^{T} \mathbf{\Phi} - \hat{\mu}^{[n]} Q_{1}(\mathbf{\Phi})_{B^{[n+1]}}^{T} Q_{2}(\mathbf{\Phi}) \right) \mathbf{r}^{[n]} \|_{2} \\ &\leq \| \left(\mu^{[n]} \mathbf{\Phi}_{B^{[n+1]}}^{T} \mathbf{\Phi}_{B^{[n+1]}} - \hat{\mu}^{[n]} Q_{1}(\mathbf{\Phi})_{B^{[n+1]}}^{T} Q_{2}(\mathbf{\Phi})_{B^{[n+1]}} \right) \mathbf{r}_{B^{[n]}}^{[n]} \|_{2} \\ &+ \| \left(\mu^{[n]} \mathbf{\Phi}_{B^{[n+1]}}^{T} \mathbf{\Phi}_{B^{[n]} \setminus B^{[n+1]}} - \hat{\mu}^{[n]} Q_{1}(\mathbf{\Phi})_{B^{[n+1]}}^{T} Q_{2}(\mathbf{\Phi})_{B^{[n]} \setminus B^{[n+1]}} \right) \mathbf{r}_{B^{[n]} \setminus B^{[n+1]}}^{[n]} \|_{2}. \end{split}$$

$$(44)$$

Using Eqn. 32 we have

$$\| \left(\mu^{[n]} \mathbf{\Phi}_{B^{[n+1]}}^T \mathbf{\Phi}_{B^{[n+1]}} - \hat{\mu}^{[n]} Q_1(\mathbf{\Phi})_{B^{[n+1]}}^T Q_2(\mathbf{\Phi})_{B^{[n+1]}} \right) \mathbf{r}_{B^{[n+1]}}^{[n]} \|_2 \le \max(\gamma_{2s}, \hat{\gamma}_{2s}) \| \mathbf{r}_{B^{[n+1]}}^{[n]} \|_2.$$
(45)

Let now $B^{[n+1]}$ be split into two disjoint sets Γ_1 and Γ_2 , where $\Gamma_1 \cap \Gamma_2 = \emptyset$ and $|\Gamma_1|, |\Gamma_2| \leq s$. We have by Eqn. 33

$$\begin{split} \| \left(\mu^{[n]} \mathbf{\Phi}_{B^{[n+1]}}^T \mathbf{\Phi}_{B^{[n]} \setminus B^{[n+1]}} - \hat{\mu}^{[n]} Q_1(\mathbf{\Phi})_{B^{[n+1]}}^T Q_2(\mathbf{\Phi})_{B^{[n]} \setminus B^{[n+1]}} \right) \mathbf{r}_{B^{[n]} \setminus B^{[n+1]}} \|_2 &\leq \\ \left(\| \left(\mu^{[n]} \mathbf{\Phi}_{\Gamma_1}^T \mathbf{\Phi}_{B^{[n]} \setminus B^{[n+1]}} - \hat{\mu}^{[n]} Q_1(\mathbf{\Phi})_{\Gamma_1}^T Q_2(\mathbf{\Phi})_{B^{[n]} \setminus B^{[n+1]}} \right) \mathbf{r}_{B^{[n]} \setminus B^{[n+1]}} \|_2^2 \\ &+ \| \left(\mu^{[n]} \mathbf{\Phi}_{\Gamma_2}^T \mathbf{\Phi}_{B^{[n]} \setminus B^{[n+1]}} - \hat{\mu}^{[n]} Q_1(\mathbf{\Phi})_{\Gamma_2}^T Q_2(\mathbf{\Phi})_{B^{[n]} \setminus B^{[n+1]}} \right) \mathbf{r}_{B^{[n]} \setminus B^{[n+1]}} \|_2^2 \\ &\leq \sqrt{2} \max(\gamma_{2s}, \hat{\gamma}_{2s}) \| \mathbf{r}_{B^{[n]} \setminus B^{[n+1]}} \|_2. \end{split} \tag{46}$$

Combining Eqn. 45 & 46

$$\begin{split} \| \left(\mu^{[n]} \mathbf{\Phi}_{B^{[n+1]}}^{T} \mathbf{\Phi} - \hat{\mu}^{[n]} Q_{1}(\mathbf{\Phi})_{B^{[n+1]}}^{T} Q_{2}(\mathbf{\Phi}) \right) \mathbf{r}^{[n]} \|_{2} \\ &= \max(\gamma_{2s}, \hat{\gamma}_{2s}) \| \mathbf{r}_{\mathbf{B}^{[n+1]}}^{[n]} \|_{2} + \sqrt{2} \max(\gamma_{2s}, \hat{\gamma}_{2s}) \| \mathbf{r}_{\mathbf{B}^{[n]} \setminus \mathbf{B}^{[n+1]}} \|_{2} \\ &\leq \sqrt{2} \max(\| \mathbf{r}_{\mathbf{B}^{[n+1]}}^{[n]} \|_{2} + \| \mathbf{r}_{\mathbf{B}^{[n]} \setminus \mathbf{B}^{[n+1]}} \|_{2}) \\ &\leq 2 \max(\gamma_{2s}, \hat{\gamma}_{2s}) \| \mathbf{r}^{[n]} \|_{2} \end{split}$$

$$(47)$$

where the last inequality follows from the fact that $\mathbf{r}_{B^{[n+1]}}^{[n]}$ and $\mathbf{r}_{B^{[n]}\setminus B^{[n+1]}}$ are orthogonal.

(a.2) Expanding the second term in Eqn. 43

$$\begin{split} &\|(\mu^{[n]}\boldsymbol{\Phi}_{B^{[n+1]}} - \hat{\mu}^{[n]}Q_{1}(\boldsymbol{\Phi})_{B^{[n+1]}}^{T})\boldsymbol{\varepsilon}\|_{2} \\ &\leq \|(\mu^{[n]}\boldsymbol{\Phi}_{B^{[n+1]}} - \hat{\mu}^{[n]}Q_{1}(\boldsymbol{\Phi})_{B^{[n+1]}}^{T})\mathbf{e}\|_{2} + \|(\mu^{[n]}\boldsymbol{\Phi}_{B^{[n+1]}} - \hat{\mu}^{[n]}Q_{1}(\boldsymbol{\Phi})_{B^{[n+1]}}^{T})\boldsymbol{\Phi}(\mathbf{x} - \mathbf{x}^{s})\|_{2}. \end{split} \tag{48}$$

Using Eqn. 30, 31 & 32 we have

$$\begin{split} &\|(\mu^{[n]}\boldsymbol{\Phi}_{B^{[n+1]}} - \hat{\mu}^{[n]}Q_{1}(\boldsymbol{\Phi})_{B^{[n+1]}}^{T})\mathbf{e}\|_{2} \leq \max((1+\gamma_{2s})/\beta_{2s} - 1/\hat{\beta}_{2s}, (1+\hat{\gamma}_{2s})/\hat{\beta}_{2s} - 1/\beta_{2s})\|\mathbf{e}\|_{2} \\ &\|(\mu^{[n]}\boldsymbol{\Phi}_{B^{[n+1]}} - \hat{\mu}^{[n]}Q_{1}(\boldsymbol{\Phi})_{B^{[n+1]}}^{T})\boldsymbol{\Phi}(\mathbf{x} - \mathbf{x}^{s})\|_{2} \\ &\leq \left(\|(\mu^{[n]}\boldsymbol{\Phi}_{\Gamma_{1}} - \hat{\mu}^{[n]}Q_{1}(\boldsymbol{\Phi})_{\Gamma_{1}}^{T})\boldsymbol{\Phi}(\mathbf{x} - \mathbf{x}^{s})\|_{2}^{2} + \|(\mu^{[n]}\boldsymbol{\Phi}_{\Gamma_{2}} - \hat{\mu}^{[n]}Q_{1}(\boldsymbol{\Phi})_{\Gamma_{2}}^{T})\boldsymbol{\Phi}(\mathbf{x} - \mathbf{x}^{s})\|_{2}^{2}\right)^{1/2} \\ &\leq \sqrt{2}\max(\hat{\gamma}_{2s}, \hat{\gamma}_{2s})\left[\|\mathbf{x} - \mathbf{x}^{s}\|_{2} + \frac{\|\mathbf{x} - \mathbf{x}^{s}\|_{1}}{\sqrt{s}}\right]. \end{split} \tag{49}$$

Combining results obtained in Eqn. 49

$$\|(\mu^{[n]}\boldsymbol{\Phi}_{B^{[n+1]}} - \hat{\mu}^{[n]}Q_{1}(\boldsymbol{\Phi})_{B^{[n+1]}}^{T})\boldsymbol{\varepsilon}\|_{2} \leq \max((1+\gamma_{2s})/\beta_{2s} - 1/\hat{\beta}_{2s}, (1+\hat{\gamma}_{2s})/\hat{\beta}_{2s} - 1/\beta_{2s})\|\mathbf{e}\|_{2} + \sqrt{2}\max(\hat{\gamma}_{2s}, \hat{\gamma}_{2s})\left[\|\mathbf{x} - \mathbf{x}^{s}\|_{2} + \frac{\|\mathbf{x} - \mathbf{x}^{s}\|_{1}}{\sqrt{s}}\right].$$
(50)

(a.3) The third term of Eqn. 43

$$\mathbb{E}[\|\hat{\mu}^{[n+1]}Q_{1}(\mathbf{\Phi})_{B^{[n+1]}}^{T}\boldsymbol{\epsilon}_{y}\|_{2}] \stackrel{(1)}{\leq} \frac{(1+\hat{\gamma}_{2s})}{\hat{\beta}_{2s}}\mathbb{E}[\|\boldsymbol{\epsilon}_{y}\|_{2}] \\
\stackrel{(2)}{\leq} \frac{(1+\hat{\gamma}_{2s})\sqrt{M}}{\hat{\beta}_{2s}2^{b_{\mathbf{y}}-1}}.$$
(51)

where the inequalities follows from (1) Eqn. 19 & 20, and (2) Lemma 3.

(a.4) Combining with Eqn. 19 & 21, Cauchy-Bunyakovsky-Schwarz, Jensen inequalities and the similar discussion above

$$\mathbb{E}[\|\hat{\mu}^{[n]}Q_{1}(\mathbf{\Phi})_{B^{[n+1]}}^{T}(\mathbf{\Phi} - Q_{2}(\mathbf{\Phi}))\mathbf{x}^{s}\|_{2}] \leq \frac{(1+\hat{\gamma}_{2s})}{\hat{\beta}_{2s}}\mathbb{E}[\|(\mathbf{\Phi} - Q_{2}(\mathbf{\Phi}))\mathbf{x}^{s}\|_{2}] \\
\leq \frac{(1+\hat{\gamma}_{2s})}{\hat{\beta}_{2s}}\sqrt{\sum_{i}^{M}\sum_{j}^{N}\mathbb{E}[(\mathbf{\Phi}_{i,j} - Q_{2}(\mathbf{\Phi}_{i,j})\mathbf{x}_{j}^{s})^{2}]} \\
= \frac{(1+\hat{\gamma}_{2s})}{\hat{\beta}_{2s}}\sqrt{\sum_{i=1}^{M}\sum_{j=1}^{N}\frac{1}{2^{2(b_{\Phi}-1)}}(\mathbf{x}_{j}^{s})^{2}} \\
= \frac{(1+\hat{\gamma}_{2s})}{\hat{\beta}_{2s}}\sqrt{\sum_{i=1}^{M}\frac{1}{2^{2(b_{\Phi}-1)}}\|\mathbf{x}^{s}\|_{2}^{2}} \\
= \frac{(1+\hat{\gamma}_{2s})\sqrt{M}}{\hat{\beta}_{2s}2^{b_{\Phi}-1}}\|\mathbf{x}^{s}\|_{2}.$$
(52)

(b) Finally, we bound the second term on the right hand side of Eqn. 42 as follows.

$$\|\mathbf{a}_{B^{[n+1]}}^{[n+1]} - \mathbf{x}_{B^{[n+1]}}^{s}\|_{2} = \|\hat{\mathbf{x}}_{B^{[n+1]}}^{[n]} + \mu^{[n]} \boldsymbol{\Phi}_{B^{[n+1]}}^{T} (\mathbf{y} - \boldsymbol{\Phi} \hat{\mathbf{x}}^{[n]}) - \mathbf{x}_{B^{[n+1]}}^{s}\|_{2}$$

$$= \|\hat{\mathbf{x}}_{B^{[n+1]}}^{[n]} + \mu^{[n]} \boldsymbol{\Phi}_{B^{[n+1]}}^{T} (\boldsymbol{\Phi} \mathbf{x}^{s} + \boldsymbol{\varepsilon} - \boldsymbol{\Phi} \hat{\mathbf{x}}^{[n]}) - \mathbf{x}_{B^{[n+1]}}^{s}\|_{2}$$

$$= \|\mathbf{r}_{B^{[n+1]}}^{[n]} - \mu^{[n]} \boldsymbol{\Phi}_{B^{[n+1]}}^{T} (\boldsymbol{\Phi} \mathbf{r}^{[n]} - \boldsymbol{\varepsilon})\|_{2}$$

$$= \|\mathbf{r}_{B^{[n+1]}}^{[n]} - \mu^{[n]} \boldsymbol{\Phi}_{B^{[n+1]}}^{T} (\boldsymbol{\Phi}_{B^{[n+1]}} \mathbf{r}_{B^{[n+1]}}^{[n]} + \boldsymbol{\Phi}_{B^{[n]} \setminus B^{[n+1]}} \mathbf{r}_{B^{[n]} \setminus B^{[n+1]}}^{[n]} - \boldsymbol{\varepsilon})\|_{2}$$

$$\leq \|(\mathbf{I} - \mu^{[n]} \boldsymbol{\Phi}_{B^{[n+1]}}^{T} \boldsymbol{\Phi}_{B^{[n+1]}}) \mathbf{r}_{B^{[n+1]}}^{[n]} \|_{2}$$

$$+ \|\mu^{[n]} \boldsymbol{\Phi}_{B^{[n+1]}}^{T} \boldsymbol{\Phi}_{B^{[n+1]}} \boldsymbol{\sigma}_{B^{[n+1]}}^{[n]} \mathbf{r}_{B^{[n]} \setminus B^{[n+1]}}^{[n]} \|_{2}$$

$$+ \|\mu^{[n]} \boldsymbol{\Phi}_{B^{[n+1]}}^{T} \boldsymbol{\varepsilon}\|_{2}. \tag{53}$$

It can easily be verified that

$$\begin{split} \|(\mathbf{I} - \boldsymbol{\mu}^{[n]} \boldsymbol{\Phi}_{B^{[n+1]}}^T \boldsymbol{\Phi}_{B^{[n+1]}}) \mathbf{r}_{B^{[n]}}^{[n]} \|_2 &\overset{(1)}{\leq} \gamma_{2s} \| \mathbf{r}_{B^{[n+1]}}^{[n]} \|_2 \\ \|\boldsymbol{\mu}^{[n]} \boldsymbol{\Phi}_{B^{[n+1]}}^T \boldsymbol{\Phi}_{B^{[n]} \backslash B^{[n+1]}} \mathbf{r}_{B^{[n]} \backslash B^{[n+1]}}^{[n]} \|_2 &\leq \left(\|\boldsymbol{\mu}^{[n]} \boldsymbol{\Phi}_{\Gamma_1}^T \boldsymbol{\Phi}_{B^{[n]} \backslash B^{[n+1]}} \mathbf{r}_{B^{[n]} \backslash B^{[n+1]}}^{[n]} \|_2^2 \right. \\ & + \|\boldsymbol{\mu}^{[n]} \boldsymbol{\Phi}_{\Gamma_2}^T \boldsymbol{\Phi}_{B^{[n]} \backslash B^{[n+1]}} \mathbf{r}_{B^{[n]} \backslash B^{[n+1]}}^{[n]} \|_2^2 \\ &\overset{(2)}{\leq} \sqrt{2} \gamma_{2s} \| \mathbf{r}_{B^{[n]} \backslash B^{[n+1]}}^{[n]} \|_2 \\ \|\boldsymbol{\mu}^{[n]} \boldsymbol{\Phi}_{B^{[n+1]}}^T \varepsilon \|_2 &\overset{(3)}{\leq} \frac{\gamma_{2s} + 1}{\beta_{2s}} \| \mathbf{e} \|_2 + \sqrt{2} (\gamma_{2s} + 1) [\|\mathbf{x} - \mathbf{x}^s\|_2 - \frac{\|\mathbf{x} - \mathbf{x}^s\|_1}{\sqrt{s}}] \\ &(54) \end{split}$$

where (1) and (2) follow from Lemma 1, (3) is derived in 49.

By the orthogonality between $\mathbf{r}_{B^{[n+1]}}^{[n]}$ and $\mathbf{r}_{B^{[n]}\setminus B^{[n+1]}}^{[n]}$, Eqn. 53 can further be simplified to

$$\|\mathbf{a}_{B^{[n+1]}}^{[n+1]} - \mathbf{x}_{B^{[n+1]}}^{s}\|_{2}|\mathbf{x}^{[n]}| \le 2\gamma_{2s}\|\mathbf{r}^{[n]}\|_{2} + \frac{\gamma_{2s}+1}{\beta_{2s}}\|\mathbf{e}\|_{2} + \sqrt{2}(\gamma_{2s}+1)\left[\|\mathbf{x} - \mathbf{x}^{s}\|_{2} - \frac{\|\mathbf{x} - \mathbf{x}^{s}\|_{1}}{\sqrt{s}}\right]. \tag{55}$$

Combining (a) and (b), the norm of recovery error is given by

$$\mathbb{E}[\|\mathbf{r}^{[n+1]}\|_{2}|\mathbf{r}^{[0]} = -\mathbf{x}^{s}] \leq 8\max(\gamma_{2s}, \hat{\gamma}_{2s})\|\mathbf{r}^{[n]}\|_{2} \\
+ 2\left(\max((1+\gamma_{2s})/\beta_{2s} - 1/\hat{\beta}_{2s}, (1+\hat{\gamma}_{2s})/\hat{\beta}_{2s} - 1/\beta_{2s}) + \frac{1+\gamma_{2s}}{\beta_{2s}}\right)\|\mathbf{e}\|_{2} \\
+ 2\sqrt{2}(1+2\max(\gamma_{2s}, \hat{\gamma}_{2s}))\left[\|\mathbf{x} - \mathbf{x}^{s}\|_{2} + \frac{\|\mathbf{x} - \mathbf{x}^{s}\|_{1}}{\sqrt{s}}\right] + 2\frac{(1+\hat{\gamma}_{2s})\sqrt{M}}{\hat{\beta}_{2s}2^{b_{\Phi}-1}}\|\mathbf{x}^{s}\|_{2} \\
+ 2\frac{(1+\hat{\gamma}_{2s})\sqrt{M}}{\hat{\beta}_{2s}2^{b_{\nu}-1}} \tag{56}$$

If $\max(\gamma_{2s}, \hat{\gamma}_{2s}) \leq 1/16$, we have

$$\mathbb{E}[\|\mathbf{r}^{[n+1]}\|_{2}|\mathbf{r}^{[0]} = -\mathbf{x}^{s}] \leq \frac{1}{2}\|\mathbf{r}^{[n]}\|_{2} + \frac{5}{\beta_{2s}}\|\mathbf{e}\|_{2} + 3.2\left[\|\mathbf{x} - \mathbf{x}^{s}\|_{2} + \frac{\|\mathbf{x} - \mathbf{x}^{s}\|_{1}}{\sqrt{s}}\right] + \frac{2.5\sqrt{M}}{\hat{\beta}_{2s}}(\|\mathbf{x}^{s}\|_{2}/2^{b_{\Phi}-1} + 1/2^{b_{\mathbf{y}}-1}).$$
(57)

$$\mathbb{E}[\|\hat{\mathbf{x}}^{[n+1]} - \mathbf{x}^{s}\|_{2}|\hat{\mathbf{x}}^{[0]} = \mathbf{0}] \leq 2^{-n} \|\mathbf{x}^{s}\|_{2} + \frac{10}{\beta_{2s}} \|\mathbf{e}\|_{2} + 6.4 \left[\|\mathbf{x} - \mathbf{x}^{s}\|_{2} + \frac{\|\mathbf{x} - \mathbf{x}^{s}\|_{1}}{\sqrt{s}} \right] + \frac{5\sqrt{M}}{\hat{\beta}_{2s}} (\|\mathbf{x}^{s}\|_{2}/2^{b_{\Phi}-1} + 1/2^{b_{y}-1}).$$
(58)

Proof of Corollary 1

The point source assumption implies that the signal is naturally sparse such that $\mathbf{x} = \mathbf{x}^s$. Let also σ_n^2 is the variance of noise corrupting antennas. Referring to Section 6, $\|\mathbf{e}\|_2 = \sqrt{L}\sigma_n$. Hence if α_{2s} , $\hat{\alpha}_{2s} \leq 1/16$, substituting these into Eqn. 58, low precision IHT recovers \mathbf{x} with accuracy

$$\mathbb{E}[\|\mathbf{x}^{n+1} - \mathbf{x}^s\|_2] \le 2^{-n} \|\mathbf{x}^s\|_2 + 10(\frac{\sqrt{L}}{\beta_{2s}} \sigma_n + \frac{L}{\hat{\beta}_{2s}} \epsilon_{\text{sky}})$$

$$\tag{59}$$

where $\epsilon_{\rm sky} = \|\mathbf{x}^s\|_2 / 2^{b_{\Phi}} + 1/2^{b_{y}}$.

Remark 4. Clearly from the above derivations, Eqn. 59 holds for the deterministic quantization as well.

Toy Example: Gaussian Data

We also investigate the performance of low precision IHT on a toy example: when data points are drawn from Gaussian distribution. Comparison of normalized IHT to other state-of-art methods is performed, for example, in (Blumensath & Davies, 2010; Blumensath et al., 2012). For Gaussian matrices, it is well know that they satisfy the restricted isometry property with high probability. Motivated by this, we apply low precision IHT to a data set where observations, entries of measurement matrix and noise are independently drawn from a zero mean and unit variance Gaussian distribution. We compute the recovery error and exact support recovery over 100 realizations of data where $\Phi \in \mathbb{R}^{256 \times 512}$ and $\mathbf{y}, \mathbf{e} \in \mathbb{R}^{256}$ at different SNR levels. The results are demonstrated in Fig. 7. 2&8 bit IHT performs slightly worse on Gaussian data, however is robust to noise as good as 32 bit IHT.

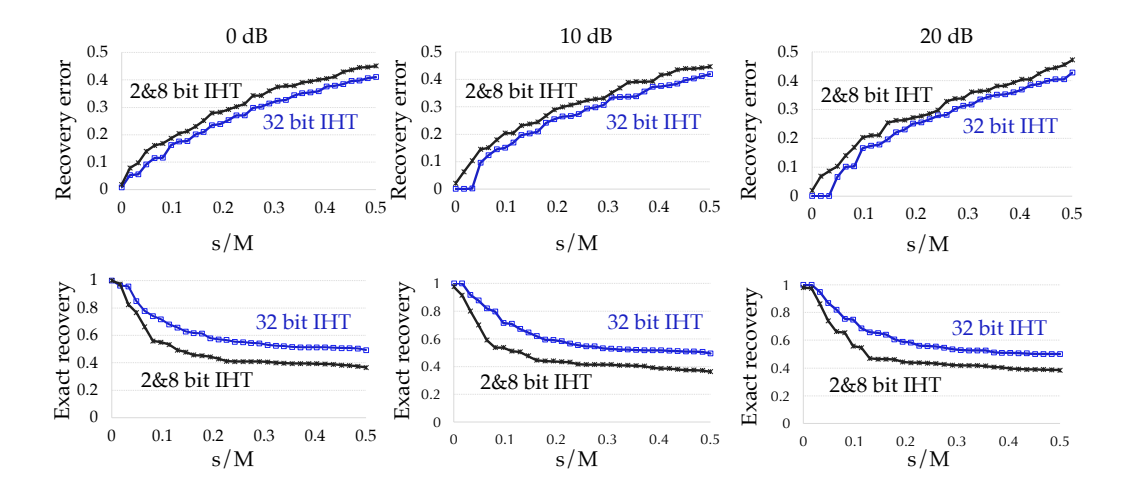


FIG 7. Comparison of 268 bit IHT to 32 bit IHT on Gaussian distributed data. The results are averaged over 100 realizations. Recovery error is calculated by $\|\mathbf{x}^{[n]} - \mathbf{x}^s\|_2 / \|\mathbf{x}^s\|_2$ and exact recovery is given by the ratio between the cardinalities of recovered support and true support.

Radio Interferometer Pipeline

Antennas at various locations on the ground records radio waves coming from the sources in space, and then send those to *interferometers* (correlator unit), which first estimate correlation between the time series-measurements so-called visibilities. Then the central processor estimates the sky image with a specified imaging technique, i.e., CLEAN (Hogbom, 1974) and A(W)-projection (Bhatganar et al., 2008).

Basic Data Model

Let us start with the following modeling assumptions: (Taylor et al., 1999)

- 1. Celestial sources are in far field, the series emanating from sources and captured by the antennas are thus paralel,
- 2. series emitted by celestial sources are narrow band zero mean circularly-symmetric complex Gaussian processes,
 - 3. series originating from different directions in the sky are uncorrelated.
- (1) follows from the assumption sources lie on a hypothetical sphere, the so-called celestial sphere. This implies that we can not measure how far the sources are.

Let $\hat{s}(t, \mathbf{r})$ denote the series emitted by the source coming from the direction $\mathbf{r} \in \mathbb{S}^2$. (2), therefore, implies $\hat{s}(t, \mathbf{r}) \sim \mathbb{C}\mathcal{N}(0, I(\mathbf{r}))$ where $I(\mathbf{r})$ is the intensity of the source series emanating from direction \mathbf{r} . Given the center frequency $f_0 \in \mathbb{R}$, (2) yields the following baseband representation of $\hat{s}(t, \mathbf{r})$:

$$s(t, \mathbf{r}) = \hat{s}(t, \mathbf{r})e^{j2\pi f_0 t}.$$
(60)

Note also that $\mathbb{E}[s(t, \mathbf{r}_1)s^*(t, \mathbf{r}_2)] = 0$, $\forall \mathbf{r}_1, \mathbf{r}_2 \in \mathbb{S}^2$ follows from (3), where * denotes the conjugate operator. The series coming from direction \mathbf{r} and recorded by antenna i is thus given by:

$$x_i(t, \mathbf{r}) = s(t - \tau_i(\mathbf{r}), \mathbf{r}) \tag{61}$$

where $\tau_i(\mathbf{r})$ denotes the time delay for the series reaching from the source to reach at the antenna *i*. Combining Eqn. 60 and 61 we have

$$x_i(t, \mathbf{r}) = \hat{s}(t - \tau_i(\mathbf{r}), \mathbf{r})e^{j2\pi f_0(t - \tau_i(\mathbf{r}))}.$$
(62)

The above derivations concern merely a specific source. Let now focus on the series measured by the antenna i coming from multiple sources (from all directions). It is then by the following integral:

$$x_i(t) = \iint_{\mathbb{S}^2} \hat{s}(t - \tau_i(\mathbf{r}), \mathbf{r}) e^{j2\pi f_0(t - \tau_i(\mathbf{r}))} d\mathbf{r}.$$
 (63)

As correlations between the antenna time-series are of special interest of imaging, let us have a closer look at the algebraic equations regarding the correlations. Recall that the source series coming from different directions in space are uncorrelated. Using this, we have the following closed-form expression:

$$\mathbb{E}[x_i(t)x_k(t)^*] = \iint_{\mathbb{S}^2} \mathbb{E}[\hat{s}(t - \tau_i(\mathbf{r}), \mathbf{r})\hat{s}^*(t - \tau_k(\mathbf{r}), \mathbf{r})]e^{-j2\pi f_0(\tau_i(\mathbf{r}) - \tau_k(\mathbf{r}))}d\mathbf{r}$$
(64)

where i and k denote different antennas. By the assumption of (2), the series $\hat{s}(t, \mathbf{r})$ remains constant over the time shift we further have

$$\mathbb{E}[x_i(t)x_k(t)^*] = \iint_{\mathbb{S}^2} I(\mathbf{r})e^{-j2\pi f_0(\tau_i(\mathbf{r}) - \tau_k(\mathbf{r}))} d\mathbf{r}$$
(65)

where $I(\mathbf{r})$ denotes the variance of the series emitted from direction \mathbf{r} referred to as sky image. We further have

$$\tau_i(\mathbf{r}) = \frac{1}{c} \langle \mathbf{r}_{\text{norm}}, \mathbf{p}_i \rangle \tag{66}$$

where $\mathbf{r}_{\text{norm}} = \frac{\mathbf{r}}{\|\mathbf{r}\|_2}$ and \mathbf{p}_i denotes the position of antenna *i*. The above relation together with Eqn. 65 gives us that

$$\mathbb{E}[x_i(t)x_k(t)^*] = \iint_{\mathbb{S}^2} I(\mathbf{r})e^{-j2\pi\frac{f_0}{c}\langle \mathbf{r}_{\text{norm}}, \ \mathbf{p}_i - \mathbf{p}_k \rangle} d\mathbf{r}.$$
 (67)

Note that $\frac{f_0}{c} = \frac{1}{\lambda_0}$ where λ_0 is the wavelength of the observation, Eqn. 67 can be further simplified to the following equation:

$$\mathbb{E}[x_i(t)x_k(t)^*] = \iint_{\Omega} I(\mathbf{r})e^{-j2\pi\langle \mathbf{r}_{\text{norm}}, \frac{\mathbf{p}_i - \mathbf{p}_k}{\lambda_0}\rangle} d\mathbf{r}$$
(68)

so-called measurement equation.

Consider now a specific region of interest centered around \mathbf{r}_0 and basis vectors $\hat{\mathbf{e}}_1$, $\hat{\mathbf{e}}_2$ and $\hat{\mathbf{e}}_3$ where $\hat{\mathbf{e}}_1$ points in the direction of rotation of the earth, $\hat{\mathbf{e}}_3$ denotes the direction of \mathbf{r}_0 and $\hat{\mathbf{e}}_2$ is perpendicular to $\hat{\mathbf{e}}_1$ and $\hat{\mathbf{e}}_3$. \mathbf{r} can be therefore approximated to $r \approx l\hat{\mathbf{e}}_1 + m\hat{\mathbf{e}}_2 + 1\hat{\mathbf{e}}_3^{-1}$. Similarly, $\frac{\mathbf{p}_i - \mathbf{p}_k}{\lambda_0}$ can also be expressed in terms of the basis vectors, i.e., $\frac{\mathbf{p}_i - \mathbf{p}_k}{\lambda_0} = u_{i,k}\hat{\mathbf{e}}_1 + v_{i,k}\hat{\mathbf{e}}_2 + w_{i,k}\hat{\mathbf{e}}_3$. Substituting these into Eqn. 68, we get

$$\mathbb{E}[x_i(t)x_k^*(t)] = \iint_{K \subset \mathbb{R}^2} \frac{e^{-j2\pi w_{i,k}(\sqrt{1-l^2-m^2}-1)}}{\sqrt{1-l^2-m^2}} I(l,m)e^{-j2\pi(u_{i,k}l+v_{i,k}m)} \ dl \ dm \tag{69}$$

where K is the compact support of $I \in \mathbb{R}^2$. The above equation is called **tangent plane** measurement equation.

As indicated earlier, the field of view is small pointing \mathbf{r}_0 , i.e., small l and m. Hence $\frac{e^{-j2\pi w_{i,k}}}{\sqrt{1-l^2-m^2}-1}\sim 1$ and $\sqrt{1-l^2-m^2}$ term can be assumed to be constant. The above resulting representation can then be further simplified to the following:

$$\mathbb{E}[x_i(t)x_k^*(t)] = \iint_{K \subset \mathbb{R}^2} e^{-j2\pi w_{i,k}} I(l,m) e^{-j2\pi (u_{i,k}l + v_{i,k}m)} \ dldm. \tag{70}$$

Key definition: The *visibility* function is defined by removing the constant phase $e^{-j2\pi w_{i,k}}$ as follows:

$$V(u,v) \stackrel{\text{def}}{=} \iint\limits_{K \subset \mathbb{R}^2} I(l,m)e^{-j2\pi(ul+vm)} \ dldm. \tag{71}$$

Therefore, each sample of this function is given by $V(u_{i,k}, v_{i,k}) = \mathbb{E}[x_i(t)x_k^*(t)]$ the so-called *visibility* measurement.

Remark that visibility equation is an integration of the product of sky intensity and a complex exponential over the unit sphere, which can be represented as a two dimensional Fourier transform. Therefore, visibility function is equivalent to Fourier transform of the image I(l, m). This relation is known as van Cittert-Zernike theorem (Taylor et al., 1999). Consequently, the samples of V(u, v) are sufficient information for sky image recovery where each baseline gives an approximate sample from Fourier transform of the sky image. This can be mathematically stated as follows:

$$V_{i,k} \sim V(u_{i,k}, v_{i,k}) = \iint_{K \subset \mathbb{R}^2} I(l, m) e^{-j2\pi(u_{i,k}l + v_{i,k}m)} dl dm.$$
 (72)

Therefore, the sky image can be recovered by taking inverse Fourier transform of the non-uniformly samples visibility function so-called *dirty image* as follows:

$$I_d(l,m) = \mathcal{F}^{-1} \Big\{ \sum_{i,k} V(u,v) \delta(u - u_{i,k}, v - v_{i,k}) \Big\}.$$
 (73)

A closer look into the above equation reveals that dirty image is equivalent to

$$I_d(l,m) = I(l,m) * I_{db}(l,m)$$
 (74)

¹More clearly; $(\mathbf{r} - \overline{\mathbf{r}_0}) + \overline{\mathbf{r}_0} \approx l\hat{\mathbf{e}}_1 + m\hat{\mathbf{e}}_2 + l\hat{\mathbf{e}}_3$.

where

$$I_{db}(l,m) = \sum_{i,k} e^{j2\pi(u_{i,k}l + v_{i,k}m)}$$
(75)

is called *dirty beam* with k baselines ((i, k) pairs with the previous notation), $\mathbf{I}(l, m)$ is the true sky map, and * denotes convolution operator.

The imaging problem in radio astronomy can be viewed as reconstructing a sky image from estimates of its Fourier transform samples. Moreover, the problem is ill-posed as we have finite number of antennas thus the baselines. This can be tackled with up to some level by introducing a prior sky model. After having reviewed the basic data model and revealed how visibilities link to Fourier transform of the sky intensities, let us now focus on the data model from array series processing point of view.

As widely used, we (very often astronomers as well) assume a point source model for the sky (A.J. van der Veen, 2013; Taylor et al., 1999). The series measured by the antenna i denoted by $x_i(t)$ is given by:

$$x_i(t) = \sum_{q=1}^{Q} \hat{s}(t - \tau_{i,q}, \mathbf{r}_q) e^{j2\pi f_0(t - \tau_{i,q})}$$
(76)

where $\tau_{i,q}$ is the time delay at the antenna i for source q and Q denotes the number of sources

Recall that the series $\hat{s}(t,r)$ remains constant over the time shift, i.e., $\hat{s}(t-\tau_{i,q},\mathbf{r}_q) = \hat{s}(t-\tau_{k,q},\mathbf{r}_q), \forall i,k$ and hence Eqn. 76 can be simplified as follows:

$$x_{i}(t) \stackrel{(1)}{=} \sum_{q=1}^{Q} \hat{s}(t - \tau_{i,q}, \mathbf{r}_{q}) e^{j2\pi f_{0}(t - \tau_{i,q})}$$

$$\stackrel{(2)}{=} \sum_{q=1}^{Q} \hat{s}(t, \mathbf{r}_{q}) e^{j2\pi f_{0}(t - \tau_{i,q})}$$

$$\stackrel{(3)}{=} \sum_{q=1}^{Q} \hat{s}_{q}(t) e^{j2\pi f_{0}(t - \tau_{i,q})}$$

$$(77)$$

where (1) and (2) follow from the arguments above. To simplify notation, we denote $\hat{s}(t, \mathbf{r}_q)$ by $\hat{s}_q(t)$ which leads (3). By Eqn. 66, we have

$$x_i(t) = \sum_{q=1}^{Q} \hat{s}_q(t) e^{j2\pi f_0(t - \langle \mathbf{r}_q, \lambda_0 \mathbf{p}_i \rangle/c)}.$$
 (78)

Consider now that antenna series $x_i(t)$, $i \in \{1, ..., L\}$ are concatenated in a vector $\mathbf{x}(t) \in \mathbb{C}^L$. Eqn. 78 can be re-written as

$$\mathbf{x}(t) = e^{j2\pi f_0 t} \sum_{q=1}^{Q} \mathbf{a}_q \hat{s}_q(t)$$
 (79)

where $\mathbf{a_q} \in \mathbb{C}^{\mathbf{L}}$ so-called antenna steering vector is given by

$$\mathbf{a}_{\mathbf{q}} = \begin{bmatrix} e^{-j2\pi\langle \mathbf{r}_{q}, \mathbf{p}_{1} \rangle} \\ e^{-j2\pi\langle \mathbf{r}_{q}, \mathbf{p}_{2} \rangle} \\ \vdots \\ e^{-j2\pi\langle \mathbf{r}_{q}, \mathbf{p}_{L} \rangle} \end{bmatrix}$$
(80)

towards source q.

Let $\mathbf{A} \in \mathbb{C}^{L \times Q}$ denote antenna steering matrix with each column given by individual antenna steering vector \mathbf{a}_q and also $\hat{\mathbf{s}}(t)$ be vector of source series $\hat{s}_q(t)$, $q \in \{1, 2, ..., Q\}$. We then have following matrix product:

$$\mathbf{x}(t) = e^{j2\pi f_0 t} \mathbf{A}\hat{\mathbf{s}}(\mathbf{t}). \tag{81}$$

Up to now, we have introduced the data model under perfect conditions in means of noise. Real-life scenarios however are not that optimistic. Conversely, thermal noise usually has a big share in the series measured by the antennas. Let thus $\mathbf{n}(t) \in \mathbb{C}^L$ be the additive white Gaussian noise (AWGN) at the antennas. More realistic model for $\mathbf{x}(t)$ in presence of noise can be as the following:

$$\mathbf{x}(t) = e^{j2\pi f_0 t} \mathbf{A}\hat{\mathbf{s}}(\mathbf{t}) + \mathbf{n}(\mathbf{t})$$
(82)

where $\mathbf{n}(t)$ is assumed to be independently drawn from the distribution $\mathbb{C}\mathcal{N}(0, \sigma_n^2 \mathbf{I_L}), \sigma_n \in \mathbb{R}$ and \mathbf{I}_L is $L \times L$ identity matrix. Moreover, the series emitted by the sources $\hat{\mathbf{s}}(t)$ are also modelled as stochastic processes where the parameters to be estimated, i.e., $\hat{\mathbf{s}}(t) \sim \mathbb{C}\mathcal{N}(0, \Sigma_s)$ where Σ_s is the diagonal covariance matrix for the source series $\hat{\mathbf{s}}(t)$.

Let ${f V}$ account for the visibility (cross-correlation) matrix. Then

$$\mathbf{V} = \mathbb{E}[\mathbf{x}(t)\mathbf{x}^{\dagger}(t)]$$

$$= \mathbb{E}[\left(e^{j2\pi f_{0}t}\mathbf{A}\hat{\mathbf{s}}(t)\right)\left(e^{j2\pi f_{0}t}\mathbf{A}\hat{\mathbf{s}}(t)\right)^{\dagger}]$$

$$= \mathbf{A}\boldsymbol{\Sigma}_{s}\mathbf{A}^{\dagger} + \boldsymbol{\Sigma}_{n}.$$
(83)

Formation of Φ

We first form a grid of sky map by $\mathbf{I}_{l,m} \in \mathbb{R}^{r \times r}$ for $l,m \in \{1,2,...,r\}$, where r is the resolution of the map. Let $\mathbf{p}_{i,k} \in \mathbb{R}^2$ denote the two-dimensional distance between i'th and k'th antenna, and $\mathbf{r}_{l,m} \in \mathbb{R}^2$ stand for two-dimensional position of pixel in l'th row and m'th column of \mathbf{I} , respectively.

Using Eqn. 72, we can approximate the noisy visibilities by

$$\mathbf{V}_{i,k} = \sum_{l,m} \mathbf{I}_{l,m} e^{-j2\pi f_0 \langle \mathbf{p}_{i,k}, \mathbf{r}_{l,m} \rangle} + \delta_{i,k}. \tag{84}$$

Definition 1. Let $\mathbf{A} \in \mathbb{K}^{M \times N}$ be a matrix, with field \mathbb{K} . The $vec(\cdot)$ operator is defined

$$vec(\cdot): \mathbb{K}^{M \times N} \to \mathbb{K}^{MN}$$

Using above definition we can reformulate Eqn. 84 as follows.

$$y = \Phi x + e \tag{85}$$

with $\mathbf{y}, \mathbf{e} \in \mathbb{C}^M$, $\mathbf{\Phi} \in \mathbb{C}^{M \times N}$ and $\mathbf{x} \in \mathbb{R}^N$ such that $\mathbf{y} = vec(\mathbf{V})$, $\mathbf{x} = vec(\mathbf{I})$, $\mathbf{e} = vec(\mathbf{\Sigma}_n)$ and finally

$$\mathbf{\Phi}_{z,w} = e^{-j2\pi f_0 \langle \mathbf{p}_{i,k}, \mathbf{r}_{l,m} \rangle} \tag{86}$$

where
$$z = i + L(k-1)$$
, $i, k = \{1, 2, ..., L\}$ and $w = l + r(m-1)$, $l, m = \{1, 2, ..., r\}$.

Clear by its definition, the entries of Φ have unity magnitude. Moreover, when Φ is formed by using closely located antennas, the phase difference between the entries is even smaller, which suggests that, compressive sensing problem in radio inteferometry has the least desirable measurement matrix structure regarding the performance of ℓ_0 -minimization methods on such matrices. However, this will in turn be useful for our application: the bounds on γ_{2s} and $\hat{\gamma}_{2s}$ will likely be satisfied.

How we satisfy conditions on Restricted Isometry Constants?

Real-life problems usually lack of traditional RIP, that is, $\|\Phi\|_2 < 1$. The scale-invariant feature of the measurement matrix used in normalized IHT however alleviates the RIP condition and imposes a fairly mild constraint in Eqn. 19, i.e., non-symmetric RIP. In a series of paper (Blumensath & Davies, 2010; Blumensath et al., 2012), CoSaMP is shown to perform markedly worse when the RIP condition fails. IHT, however, still preserves its near-optimal recoveries far beyond the region of RIP. Recall from the main paper that the step size $\hat{\mu}^{[n]}$ is required to counteract the scaling of $\hat{\Phi}$ such that $\|\hat{\mu}^{0.5}\hat{\Phi}\|_2^2 < 1$ to ensure the convergence. The adaptive step size setting of normalized IHT yields the trivial bound on μ as (Blumensath et al., 2012)

$$1/\hat{\beta}_{2s}^2 \le 1/\hat{\beta}_s^2 < \hat{\mu}^{[n]} < 1/\hat{\alpha}_s^2 \le 1/\hat{\alpha}_{2s}^2. \tag{87}$$

Convergence is trivial in low precision setting provided that $\hat{\mu}^{[n]}$ is chosen adaptively according to strategy introduced by (Blumensath & Davies, 2010). Regarding performance guarantees, however, in Theorem 3 we show that if $\gamma_{2s} = \beta_{2s}/\alpha_{2s} - 1$, $\hat{\gamma}_{2s} = \hat{\beta}_{2s}/\hat{\alpha}_{2s} - 1 \le 1/16$, then the recovery error inversely scales with β_{2s} and $\hat{\beta}_{2s}$, which we can up-scale hence reduce the error. We previously sketch the values of β_{2s} and $\hat{\beta}_{2s}$ for the current setting in our paper and show that they are large enough to diminish recovery error and no upscale is necessity in radio astronomy case. Yet, for provable guarantees, yet, we need to satisfy the conditions on γ_{2s} and $\hat{\gamma}_{2s}$. Clearly, this cannot be done by re-scaling β_{2s} and $\hat{\beta}_{2s}$ because α_{2s} and $\hat{\alpha}_{2s}$ will be scaled accordingly by the same weight. Therefore it remains to use a more sophisticated technique to achieve this. We claim that there exist possible deterministic transformations that can be applied on Φ . However, in radio astronomy, we have the flexibility to ensure the conditions on γ_{2s} and $\hat{\gamma}_{2s}$ holds as follows.

Let us form a grid on [l,m], $l,m\in[-d,d]$ where the sky map is displayed. By changing d, we claim that the bounds on γ_{2s} and $\hat{\gamma}_{2s}$ can be tuned. Given the antenna locations,

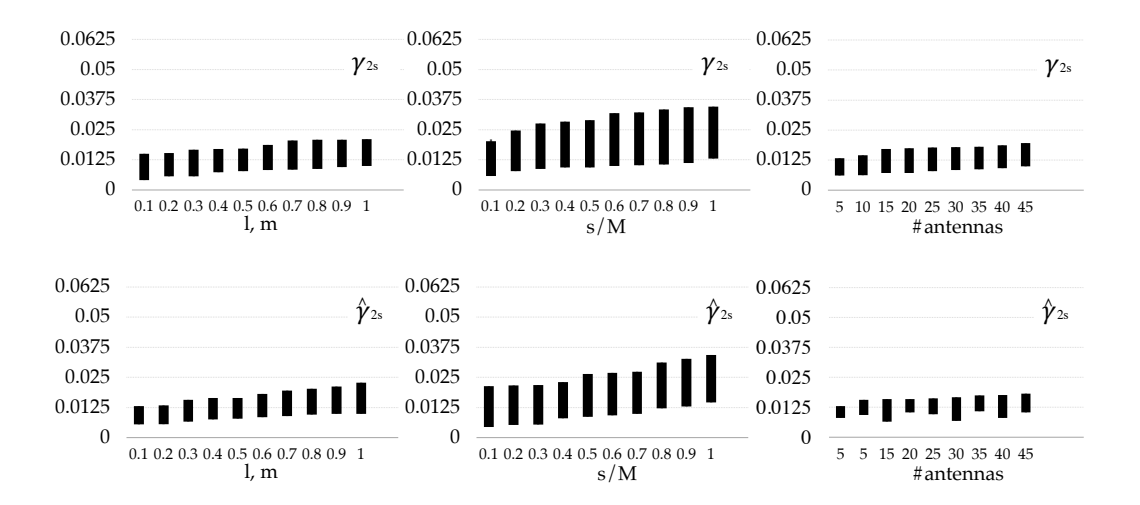


FIG 8. The change of γ_{2s} and $\hat{\gamma}_{2s}$ with grid boundaries l and m, the sparsity ratio s/M and the number of antennas. For all cases, the conditions on γ_{2s} and $\hat{\gamma}_{2s}$ are satisfied. For each box, 1000 realizations of \mathbf{x} are drawn from a normal distribution and the largest and smallest $\|\mathbf{\Phi}\mathbf{x}\|_2/\|\mathbf{x}\|_2$ is computed to estimate γ_{2s} , and this is repeated 100 times to have a numerical range of possible γ_{2s} values.

we can compute Φ that ensures the conditions with high probability. Fig. 8 illustrates the numerical experiments conducted in the current setting where we recover the sky map with resolution of 256 pixels per axis. The numerical results suggest that these conditions in the certain settings and can be further refined with parameter d. Yet, everything comes with its own cost. The disadvantage of this strategy lies in the meaning of d, that is, d limits the field of view the antennas observe. Luckily, it is not a practical concern as the limits of d can be known a priori given number and the locations of antennas. Also, when we increase d drastically to enlarge the field of view and no longer observe a sky source in the outer field, it already hints on the practical range of d for the respective setting. In our setting, practical range of d is contained in [0,1]. The conditions on γ_{2s} and $\hat{\gamma}_{2s}$ are satisfied in our setting with high probability. The effect of antenna numbers and sparsity level are also illustrated in Fig. 8. Increase in the sparsity ratio s/M and d leads a slight increase in γ_{2s} and $\hat{\gamma}_{2s}$. However, we can control this and adjust accordingly to satisfy the conditions. The values of γ_{2s} and $\hat{\gamma}_{2s}$ are naturally satisfied in our settings, i.e., γ_{2s} , $\hat{\gamma}_{2s} \leq 1/16 = 0.0625$.

Inverse Fourier transform combined with CLEAN algorithm

Referring to Eqn. 74 & 75, current imaging techniques first performs naive inverse Fourier transform of the visibilities such that

$$\mathbf{I}_{d}(l,m) = \sum_{i,j} V(u_{i,j}, v_{i,j}) e^{j2\pi(u_{i,j}l + v_{i,j}m)}.$$
(88)

CLEAN algorithm (a deconvolution algorithm) therefore takes the dirty image $\mathbf{I}_d(l,m)$

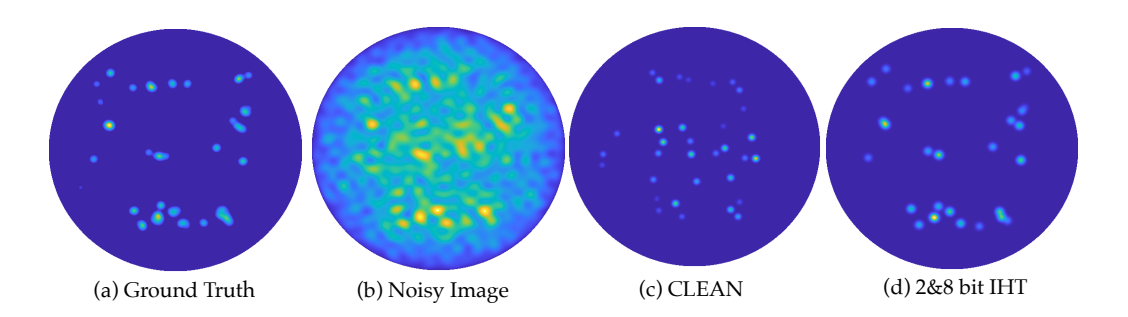


Fig 9. Comparison of 268 bit IHT to CLEAN Algorithm. The CLEAN mostly captures the noise artefacts as actual sources unlike IHT.

as input and outputs a sparse sky map by iteratively removing a fraction² of the highest peak convolved with the *dirty beam* $\mathbf{I}_{db}(\mathbf{l}, \mathbf{m})$.

Recall from the discussions in the main paper that noise in receivers is far stronger than the weak incoming signals thus low SNR at the antenna level results, i.e., usually ranged from -5 to 5 dB. In Fig. 9, we apply the CLEAN algorithm to the LOFAR data set we use throughout the main paper, where SNR is computed nearly 0 dB. This particular experiment states that the CLEAN algorithm notably underperforms in the presence of significant noise. This undesirable property is yet not surprising. A careful look into the the algorithmic steps, it apparently matches also to the noise artefacts in the image considering them as a point source. This can also be justified mathematically: we designed the problem such that an execution of CLEAN corresponds to the first iteration recovery of IHT, which interprets our numerical results.

Computationally, the CLEAN requires a 2D Fourier inversion and deconvolution per iteration thus the operational expense of the method is relatively higher compared to those of IHT and CoSaMP.

References

Ai, A., Lapanowski, A., Plan, Y., and Vershynin, R. One-bit compressed sensing with non-gaussian measurements. *arXiv:1208.6279*, 2012.

A.J. van der Veen, S.J. Wijinholds. Signal processing tools for radio astronomy. *Handbook of Signal Processing Systems*, 2013.

Alistarh, D., Li, J., Tomioka, R., and Vojnovic, M. Qsgd: Randomized quantization for communication-optimal stochastic gradient descent. arXiv:1610.02132, 2016.

Bhatganar, S., Cornwell, T., Golap, T. J., and Uson, J. M. Correcting direction-dependent gains in the deconvolution of radio interferometric images. *Astronomy and Astrophysics*, 487:419–429, 2008.

Blanchard, J. D., Tanner, J., and Wei, K. Conjugate gradient iterative hard thresholding: Observed noise stability for compressed sensing. *Oxford Numerical analysis group preprin*, 2013

²so-called loop gain ≤ 0.3

- Blumensath, T. Accelerated iterative hard thresholding. The Journal of Fourier Analysis and Applications, 92(3):265–274, 2012.
- Blumensath, T. Compressed sensing with nonlinear observations and related nonlinear optimization problems. *IEEE Transactions of Information Theory*, 59(6):3466–3474, 2013.
- Blumensath, T. and Davies, M.E. Iterative thresholding for sparse approximations. *The Journal of Fourier Analysis and Applications*, 14(5-6):629–654, 2008.
- Blumensath, T. and Davies, M.E. Iterative thresholding for compressed sensing. *Applied and Computational Harmonic Analysis*, 27(3):265–274, 2009.
- Blumensath, T. and Davies, M.E. Normalized iterative hard thresholding: Guaranteed stability and performance. *IEEE Selected Topics in Signal Processing*, 4(2):298–309, 2010.
- Blumensath, T., Davies, M.E., and Rilling, G. Greedy algorithms for compressed sensing. In Y. C. Eldar, and G. Kutyniok (ed.), *Compressed Sensing: Theory and Applications*, pp. 348–393. Cambridge University Press., Cambridge, GB, 2012.
- Boufounos, P. and Baraniuk, R. G. 1-bit compressive sensing. 2009.
- Candes, E. The restricted isometry property and its implications for compressed sensing. *Comptes Rendus Mathematique*, 346(9-10):589–592, 2008.
- Candes, E. J., Romberg, J., and Tao, T. Robust uncertainty principles: Exact signal reconstruction from highly incomplete frequency information. *IEEE Transactions of Information Theory*, 52(2):489–509, 2006a.
- Candes, E. J., Romberg, J., and Tao, T. Stable signal recovery from incomplete and inaccurate measurements. *Communications on pure and applied mathematics*, 59(8):1207–1223, 2006b.
- Cevher, V. On accelerated hard thresholding methods for sparse approximation. Wavelets And Sparsity Xiv, 8138, 2011.
- Chartrand, R. and Staneva, V. Restricted isometry properties and nonconvex compressive sensing. *Inverse Problems*, 24, 2008.
- Davenport, M. A., Plan, Y., can den Berg, E., and Wooters, M. 1-bit matrix completion. arXiv:1209.3672, 2012.
- Donoho, D. L. Compressed sensing. *IEEE Transactions of Information Theory*, 52(4): 1289–1306, 2006.
- Gopi, S., Netrapalli, P., Jain, P., and Nori, A. One-bit compressed sensing: Provable support and vector recover. In *International Conference on Machine Learning*, 2013.
- Gupta, A., Nowak, R., and Recht, B. Sample complexity for 1-bit compressed sensing and sparse classification. *IEEE Internation Symposium on Information Theory*, 2010.
- Gupta, S., Agrawal, A., Gopalakrishnan, K., and Narayanan, P. Deep learning with limited numerical precision. In *International Conference on Machine Learning*, 2013.
- Hogbom, J. A. Aperture synthesis with a non-regular distribution of interferometer baselines. *Astronomy and Astrophysics Supplement*, 15:417, 1974.
- Hu, W. C. and Kaabouch, N. (eds.). Scalable data mining, archiving, and big data management for the next generation. IGI Global, 2014.
- Hubara, I., Courbariaux, M., Soudry, D., Al-Yaniv, R., and Bengio, Y. Quantized neural networks: Training neural networks with low precision weights and activations. arXiv:1609.07061, 2016.
- Jacques, L., Laska, J. N., and Boufounos, P. Robust 1-bit compressive sensing via binary stable embeddings of sparse vectors. *CORR*: 1104.3160, 2012.

- Kara, K., Alistarh, D., Alonso, G., Mutlu, O., and Zhang, C. Fpga-accelerated dense linear machine learning: A precision-convergence trade-off. In Field-Programmable Custom Computing Machines (FCCM), 2017 IEEE 25th Annual International Symposium on, pp. 160–167. IEEE, 2017.
- Laska, J. N., Wen, Z., Yin, W., and Baraniuk, R. G. Fast and accurate signal recovery from 1-bit compressive measurements. *IEEE Transactions on Signal Processing*, 59(11): 5289–5301, 2011.
- Li, F., Cornwell, T. J., and de Hoog, F. The application of compressive sampling to radio astronomy 1: Deconvolution. *Astronomy and Astrophysics Manuscript*, 15:417, 2011.
- Li, F., Zhang, B., and Liu, B. Ternary weight networks. arXiv:1605.04711, 2016.
- Liu, B., Yuan, X. T., Wang, L., Liu, Q., and Metaxas, D. N. Dual iterative hard thresholding: From non-convex sparse minimization to non-smooth concave maximization. In International Conference on Machine Learning, 2017.
- Neededl, D. and Tropp, J. A. Cosamp: Iterative signal recovery from incomplete and inaccurate samples. *Applied and Computational Harmonic Analysis*, 26(3):301–321, 2008.
- Plan, Y. and Vershynin, R. One-bit compressed sensing by linear programming. arXiv:1109.4299, 2011.
- Plan, Y. and Vershynin, R. Robust 1-bit compressed sensing and sparse logistic regression: A convex programming approach. *CORR: 1202.1212*, 2012.
- Rastegari, M., Ordonez, V., Redmon, J., and Farhadi, A. Xnor-net: Imagenet classification using binary convolutional neural networks. In *European Conference on Computer Vision*, 2016.
- Sa, C. M. De, Zhang, C., Olukotun, K., and Re, C. Taming the wild: A unified analysis of hogwild-style algorihms. In *Advances in Neural Information Processing Systems*, 2015.
- Seide, F., Fu, H., Jasha, L. G., and Yu, D. 1-bit stochastic gradient descent and application to data-parallel distributed training of speech dnns. *Interspeech*, 2014.
- Taylor, G. B., Carilli, C. L., and R. A. Perley, National Radio Astronomy Observatory. Synthesis imaging in radio astronomy ii. In ASP Conf. Series, 1999.
- Wei, K. Fast iterative hard thresholding for compressed sensing. *IEEE Signal Processing Letters*, 22(5), 2015.
- Wenger, S., Darabi, S., Sen, P., Glassmeier, K. H., and Magnor, M. Compressed sensing for aperture synthesis imaging. *International Conference on Image Processing*, 2010.
- Wiaux, Y., Jacques, L., Puy, G., Scaife, A. M. M., and Vandergheynst, P. Compressed sensing imaging techniques for radio interferometry. *Monthly Notices of the Royal Astronomical Society*, 2009.
- Yuan, X. T., Li, P., and Zhang, T. Gradient hard thresholding oursuir for sparsity-constrained optimization. In *International Conference on Machine Learning*, 2014.
- Yuan, X. T., Li, P., and Zhang, T. Exact recovery of hard thresholding pursuit. In Advances in Neural Information Processing Systems, 2016.
- Zhang, H., Li, J., Kara, K., Alistarh, D., Liu, J., and Zhang, C. Zipml: Training linear models with end-to-end low precision, and a little bit of deep learning. In *International Conference on Machine Learning*, pp. 4035–4043, 2017.
- Zhou, S., Wu, Y., Ni, Z., Zhou, X., Wen, H., and Zou, Y. Convolutional neural networks using logarithmic data representation. *arXiv:1603.01025*, 2016a.
- Zhou, S., Wu, Y., Ni, Z., Zhou, X., Wen, H., and Zou, Y. Dorefa-net: Training low bitwidth

convolutional neural networks with low bit width gradients. $arXiv:1606.06160,\,2016$ b.